

Relativistic models of two low-luminosity radio jets: B2 0326+39 and B2 1553+24

J.R. Canvin ^{*1}, R.A. Laing^{2,1}

¹ *University of Oxford, Department of Astrophysics, Denys Wilkinson Building, Keble Road, Oxford OX1 3RH*

² *European Southern Observatory, Karl-Schwarzschild-Straße 2, D-85748 Garching-bei-München, Germany,*

Received

ABSTRACT

We apply the intrinsically symmetrical, decelerating relativistic jet model developed by Laing & Bridle for 3C 31 to deep, full-synthesis 8.4-GHz VLA imaging of the two low-luminosity radio galaxies B2 0326+39 and B2 1553+24. After some modifications to the functional forms used to describe the geometry, velocity, emissivity and magnetic-field structure, these models can accurately fit our data in both total intensity and linear polarization. We conclude that the jets in B2 0326+39 and B2 1553+24 are at angles of $64^\circ \pm 5^\circ$ and $7.7^\circ \pm 1.3^\circ$ to the line of sight, respectively. In both objects, we find that the jets decelerate from $0.7 - 0.8c$ to $<0.2c$ over a distance of approximately 10 kpc, although in B2 1553+24 this transition occurs much further from the nucleus than in B2 0326+39 or 3C 31. The longitudinal emissivity profiles can be divided into sections, each fit accurately by a power law; the indices of these power laws decrease with distance from the nucleus. B2 0326+39 also requires a discontinuity in emissivity to in order to fit a region with several bright knots of emission. In B2 1553+24, the sudden brightening of the jet can be explained by a combination of rapid expansion of the jet and a continuous variation of emissivity. The magnetic fields in both objects are dominated by the longitudinal component in the high-velocity regions close to the nucleus and by the toroidal component further out, but B2 0326+39 also has a significant radial component at large distances, whereas B2 1553+24 does not. Simple adiabatic models fail to fit the emissivity variations in the regions of high velocity but provide good descriptions of the emissivity after the jets have decelerated. Given the small angle to the line of sight inferred for B2 1553+24, there should be a significant population of similar sources at less extreme orientations. Such objects should have long ($\gtrsim 200$ kpc), straight, faint jets and we show that their true sizes are likely to have been underestimated in existing images.

Key words: galaxies: jets – radio continuum:galaxies – magnetic fields – polarization – MHD

1 INTRODUCTION

Evidence that the jets in low-luminosity, FRI (Fanaroff & Riley 1974) radio galaxies are initially relativistic and decelerate on kpc scales has mounted in recent years. FRI sources are thought to be the side-on counterparts of BL Lac objects, in which relativistic motion on parsec scales is well-established (Urry & Padovani 1995). Superluminal motions have been seen on milliarc-second scales in several FRI jets (Giovannini et al. 2001) and on arcsecond scales in M 87 (Biretta, Zhou & Owen 1995). In FRI sources, the lobe containing the main

(brighter) jet is less depolarized than the counter-jet lobe (Morganti et al. 1997b). This can be explained if the main jet points toward the observer, suggesting that the brightness asymmetry is caused by Doppler beaming (Laing 1988). The asymmetry decreases with distance from the nucleus (Laing et al. 1999), implying that the jets must decelerate. Self-consistent models of the deceleration of relativistic jets by injection of matter lost from stars or entrained from the surrounding galactic atmosphere have been calculated by Bicknell (1994), Komissarov (1994) and Bowman, Leahy & Komissarov (1996).

Laing & Bridle (2002a, hereafter LB) fit VLA images of the radio jets in the nearby FRI radio galaxy 3C 31 using a sophisticated model to reproduce the observed

* E-mail: jrc@astro.ox.ac.uk

total and polarized emission within 30 arcsec of the nucleus, where the jets are straight. They parameterized the three-dimensional distributions of velocity, emissivity and magnetic-field structure, calculated the brightness at each point within the jets in Stokes I , Q and U , accounting for the effects of relativistic aberration, and integrated along the line of sight to reproduce the expected distributions on the sky. They concluded that the jets in 3C 31 could be accurately modelled as intrinsically identical, axisymmetric, antiparallel, decelerating, relativistic flows, with locally random but anisotropic magnetic fields. Optimization of the model parameters placed tight constraints on the geometry, velocity, emissivity and field structure. Laing & Bridle (2002b) used this velocity field, together with estimates of the external pressure and density from *Chandra* observations (Hardcastle et al. 2002) in a conservation-law analysis based on that of Bicknell (1994). They showed that there are self-consistent solutions for jet deceleration by injection of thermal matter and derived the variations of pressure, density, Mach number and entrainment rate along the jets. Finally, Laing & Bridle (2004) developed models of adiabatic, relativistic jets with velocity shear and applied them to 3C 31. They demonstrated that such models provide a reasonable description of the emissivity and magnetic-field variations at large distances from the nucleus but fail closer in, and inferred that significant reacceleration of relativistic particles is required precisely where X-ray synchrotron emission is observed (Hardcastle et al. 2002).

In the present paper we apply a modified version of LB's model to the jets of two FRI radio galaxies: B2 0326+39 and B2 1553+24. Our principal aim is identical to that of LB: to estimate the distributions of velocity, emissivity and magnetic-field structure without introducing preconceptions about the (poorly understood) internal physics. By studying different objects we hope to be able to improve the range of physical scales we are able to probe, to identify which intrinsic features are common to all FRI jets and which vary from object to object and to assess the dependence of the jet structure on power and environmental conditions.

Section 2 presents our new, deep, full-synthesis VLA images. In Section 3, we outline the model, emphasizing the parameterizations of the geometry, velocity, emissivity and magnetic field which differ from those used by LB. Section 4 compares our best-fitting models with the observed data in a variety of ways to show the features that we are able to reproduce as well as those we cannot. In Section 5, we present the velocity, emissivity and field structures of the best-fitting models. Section 6 investigates whether the magnetic-field structure and emissivity are consistent with the assumptions of flux freezing and pure adiabatic energy loss and examines the idea that the jets reaccelerate. We then consider the appearance of the model for B2 1553+24 at large angles to the line of sight and the implications for the detectability of side-on counterparts. Finally, we briefly compare the models for 3C 31, B2 0326+39 and B2 1553+24. Section 7 summarizes our conclusions and outlines possible avenues for further work.

We adopt a Hubble constant, $H_0 = 70 \text{ km s}^{-1} \text{ Mpc}^{-1}$ throughout and define spectral index α in the sense $S(\nu) \propto \nu^{-\alpha}$. We use the notation $p = (Q^2 + U^2)^{1/2} / I$ for the degree of linear polarization.

2 OBSERVATIONS AND IMAGES

2.1 Object selection

Our models assume that the jets are intrinsically identical, antiparallel, axisymmetric stationary flows, so any apparent differences must be due entirely to relativistic effects. Some important selection criteria are therefore imposed on our choice of source:

(i) Only straight parts of the jets can be modelled and it is therefore important that the first bends in both the main and counter-jets be as far from the nucleus as possible.

(ii) The jet and counter-jet must leave the nucleus in strictly antiparallel directions.

(iii) We derive the *sidedness ratio* by dividing a total-intensity image of the jets by a copy of itself rotated through 180° about the nucleus. The ratio is in the sense main jet/counter-jet and cannot be < 1 over a significant area if the asymmetries are to be attributed entirely to relativistic effects (we expect some local fluctuations due to small-scale structure). This excludes a few objects, in particular those where the counter-jet is wider than the main jet (e.g. B2 0755+379; Bondi et al. 2000).

(iv) There cannot be any other radio features (e.g. lobes) that could be confused with the emission from the jet.

(v) The jets must be bright enough to produce a significant polarized signal from the region to be modelled. This is required in order to break the degeneracy between velocity and angle to the line of sight which is inherent in the total intensity (Section 3.2).

We selected two suitable targets from the well studied sample of nearby radio galaxies identified with sources in the B2 catalogue (Colla et al. 1975; Parma et al. 1987).

2.2 B2 0326+39

B2 0326+39 is a typical FRI radio source associated with a bright elliptical galaxy at $z = 0.0243$ (Miller et al. 2002). Its luminosity at 1.4 GHz is $P_{1.4} = 2.2 \times 10^{24} \text{ WHz}^{-1}$. 5-GHz images from the WSRT (Parma 1982) and VLA (Bridle 1982) first resolved the two fairly symmetrical, antiparallel jets. Comprehensive observations at multiple frequencies and resolutions between 26 and 0.6 arcsec were made by Bridle et al. (1991), who showed that the main (western) jet is much brighter than the counter-jet for the first 4 arcsec from the nucleus and that the change from one-sided to two-sided structure is accompanied by a flip in the polarization from parallel to perpendicular apparent magnetic field. The surrounding lobe emission is resolved out in images with $\text{FWHM} \leq 2 \text{ arcsec}$. The mean spectral index of the jets close to the nucleus is $\alpha = 0.55$ between 1.4 and 5.0 GHz (Bridle et al. 1991).

ROSAT PSPC observations (Canosa et al. 1999) reveal a point source with a flux of 36 nJy at 1 keV and an extended atmosphere well fitted by a beta model with form factor $\beta_{\text{atm}} = 0.35$ and core radius $r_c = 30 \text{ kpc}$.

2.3 B2 1553+24

B2 1553+24 is a more distant ($z = 0.0426$; Colla et al. 1975) and less luminous ($P_{1.4} = 4.7 \times 10^{23} \text{ WHz}^{-1}$)

FRI radio galaxy. VLA observations at 1.4 and 4.8 GHz (Morganti et al. 1987) revealed two straight, well-collimated jets aligned NW – SE with very little surrounding lobe emission (see also Stocke & Burns 1987; de Ruiter et al. 1993). Faint extended emission associated with the brighter jet is visible on the NVSS, however (Condon et al. 1998). The jets are similar at large distances from the bright compact nucleus but become very asymmetric in the central 5 arcsec. Their mean spectral index is $\alpha = 0.60$ (Morganti et al. 1987). The bright radio, optical and X-ray core (Laing et al. 1999; Capetti et al. 2000; Canosa et al. 1999), the very large side-to-side asymmetries between the two jets close to the nucleus (Laing et al. 1999) and the detection of optical emission from the base of the main jet using HST (Parma et al. 2003) all indicate that the jets are close to the line of sight.

2.4 Observations and data reduction

The observations were made using the VLA with a centre frequency of 8.46 GHz and a 100-MHz bandwidth in all four standard configurations for B2 0326+39 and in A, B and C configurations for B2 1553+24 (Table 1). Either 3C 48 or 3C 286 was used as the primary calibrator for amplitude and one of 3C 138 or 3C 286 was observed to set the **E**-vector position angle. The data for each configuration were reduced separately in the AIPS software package using standard techniques of calibration, imaging and self-calibration. The datasets were then concatenated using the AIPS task DBCON starting with the widest configurations (A and B), first adjusting the core flux of the smaller-configuration dataset to match that observed with the larger configuration and imaged at matched resolution. A further iteration of phase self-calibration was done after each combination. This procedure accounts for any core flux-density variation between observations. CLEANed images were produced at three resolutions: full (FWHM 0.25 arcsec) and tapered to two lower resolutions giving better signal-to-noise ratio in the outer parts of the jets. *I* images were also produced using maximum-entropy deconvolution, first subtracting a point source at the position of the core. After the deconvolution step, the point source was added back in and the image convolved with the same truncated Gaussian beam as used in the CLEANed images. The maximum-entropy and CLEANed images were consistent apart from some low-level artefacts clearly associated with the latter. We therefore show only the maximum-entropy *I* images. The *Q* and *U* images were CLEANed. Noise levels for *I* and *Q/U* images are given in Table 2 and are close to theoretical limits. All of the displayed polarization vectors have been rotated by 90° from the direction of the **E**-vector at 8.4 GHz and therefore represent apparent *magnetic* field. No high-resolution, multifrequency studies of Faraday rotation have yet been made for the two sources, so we have not corrected for this effect. The estimates of rotation measure from two-frequency data given by Bridle et al. (1991) and Morganti et al. (1987, 1997a) and direct comparison of their higher-frequency images with ours implies that the magnetic field directions inferred from our data are in error by $<2^\circ$ due to Faraday rotation. No corrections for Ricean bias (Wardle & Kronberg 1974) have been made in deriving the images of degree of polarization, *p*, presented in this paper, but they have all been blanked at low signal-to-noise ratio as indicated in the figure captions, so the bias is

Table 1. Record of VLA observations

Object	Configuration	Date	Integration time (min)
B2 0326+39	A	1999 Sep 18	604
	B	1999 Dec 19	604
	C	2000 May 14	131
	D	2000 Aug 17	41
B2 1553+24	A	1999 Sep 18	603
	B	1999 Dec 19	321
	C	2000 May 14	107

Table 2. Image resolutions and noise levels. σ_I is the off-source noise level on the *I* image; σ_P the average of the noise levels for *Q* and *U*.

Object	FWHM (arcsec)	rms noise level ($\mu\text{Jy} / \text{beam area}$)	
		σ_I	σ_P
B2 0326+39	1.50	7.6	6.2
	0.50	5.7	6.0
	0.25	5.8	6.8
B2 1553+24	1.50	5.2	5.8
	0.75	5.7	5.7
	0.25	6.0	6.5

negligible. In any case, the fitting procedure described below (which uses the *Q* and *U* images directly) is unaffected.

2.5 Source description

The positions and 8.4-GHz flux densities of the cores found from our A-configuration images are given in Table 3.

2.5.1 B2 0326+39

Figs 1(a) – (c) show the jets of B2 0326+39 at three different resolutions. In panel (a), the jets can be seen over their full extent. They are initially straight and antiparallel, although both bend slightly (by $\approx 3^\circ$) about 25 arcsec from the nucleus. At a distance of ≈ 22 arcsec the ridge line of the main jet starts to oscillate slightly. Panel (b) shows the inner 45 arcsec of both jets at 0.5-arcsec resolution: the jets appear very different from each other within ≈ 10 arcsec of the nucleus but become almost indistinguishable further out. This is also illustrated in Fig 1(d), which shows the ratio of

Table 3. Core flux densities and positions

Object	Core flux (mJy)	Core Position (J2000)	
		RA	Dec
B2 0326+39	71.4	$03^{\text{h}}29^{\text{m}}23.887^{\text{s}}$	$39^\circ 47' 31.96''$
B2 1553+24	63.5	$15^{\text{h}}56^{\text{m}}03.912^{\text{s}}$	$24^\circ 26' 52.92''$

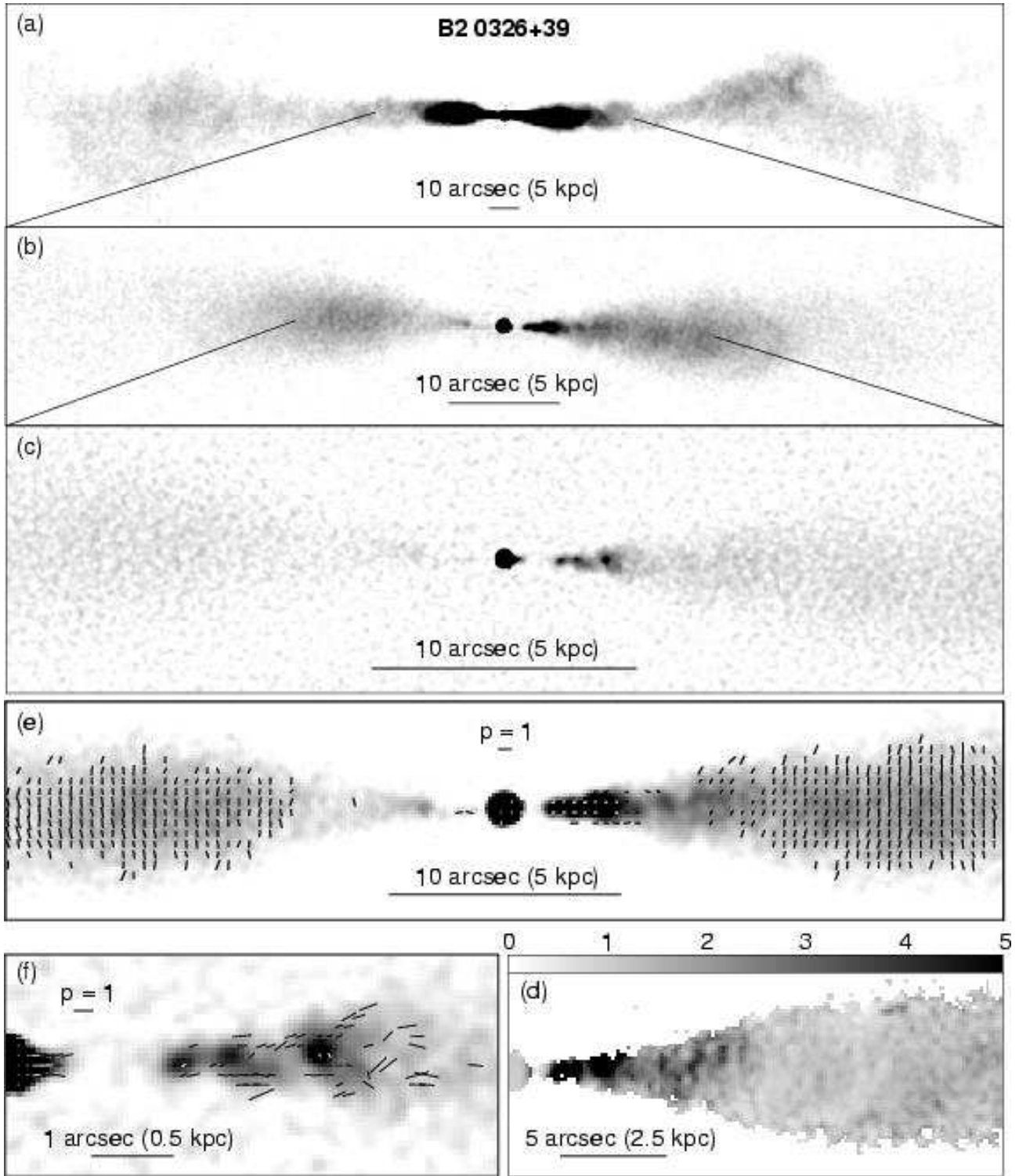


Figure 1. Montage showing the large-scale structure and jets of B20326+39 at 8.4 GHz. Panels (a) – (c) have North at the top; in the remaining panels, the images have been rotated slightly so that the jet axis is horizontal. (a) 5.7 arcmin (170 kpc) East-West field at 1.5 arcsec (0.75 kpc) resolution. (b) 1.5 arcmin (45 kpc) East-West field at 0.50 arcsec (0.25 kpc) resolution. (c) 38 arcsec (19 kpc) East-West field at 0.25 arcsec (0.13 kpc) resolution. (d) The jet/counter-jet intensity ratio (defined as in Section 2.1) for the straight region of the jet within 22 arcsec of the nucleus at 0.50 arcsec (0.25 kpc) resolution. The grey-scale range (0 – 5) is indicated by the labelled bar. (e) Grey-scale of total intensity with superimposed polarization vectors for the straight region of the jets within 22 arcsec of the nucleus at 0.50 arcsec (0.25 kpc) resolution. The lengths of the vectors are proportional to the degree of polarization p and their directions are those of the apparent magnetic field. (f) As in panel (e), but showing the inner 6 arcsec of the western jet at 0.25 arcsec (0.13 kpc) resolution.

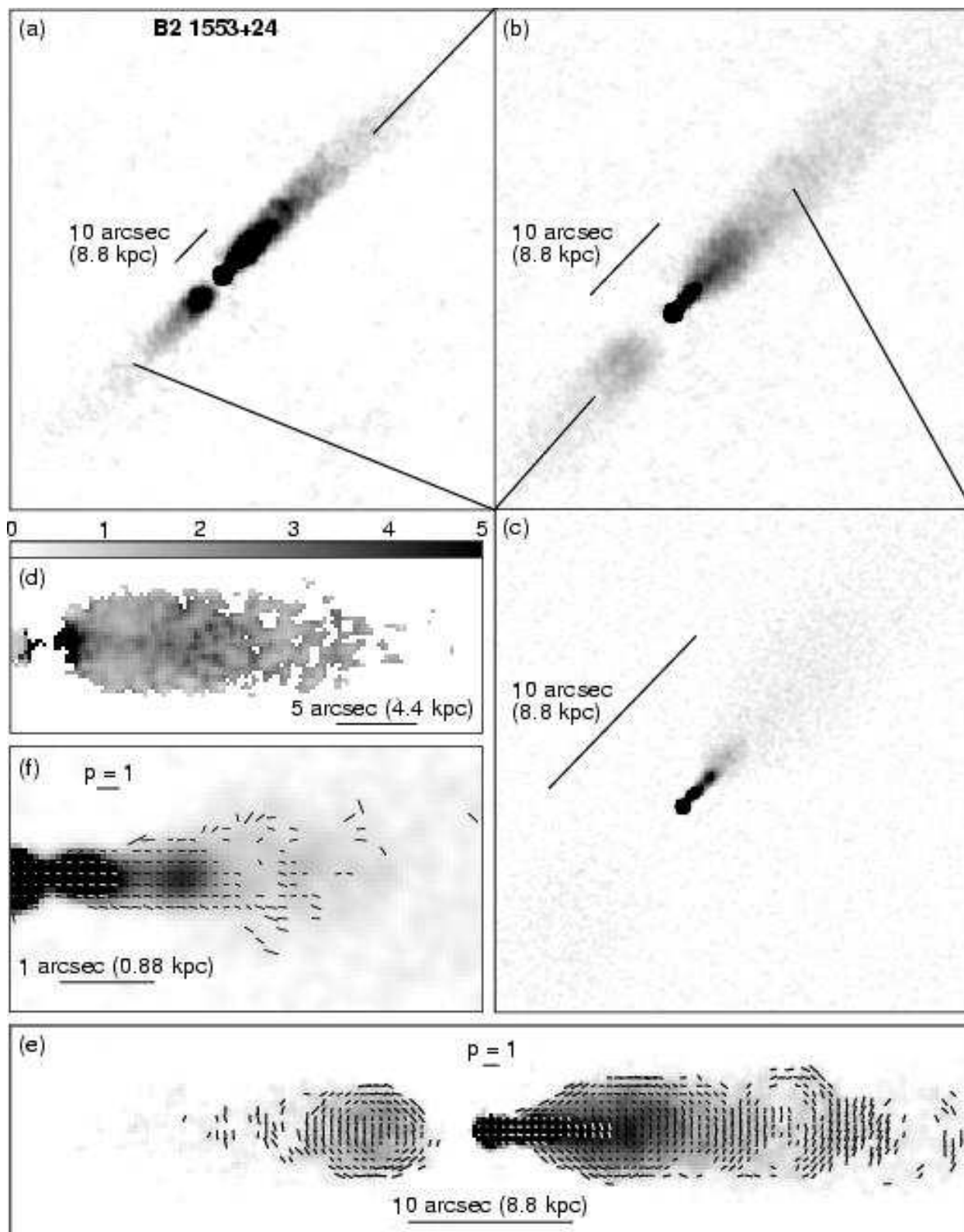


Figure 2. Montage showing the jets of B2 1553+24 at 8.4 GHz. Panels (a) – (c) show grey-scales of total intensity and have North at the top; the remaining images have been rotated so that the jet axis is horizontal. (a) 111 arcsec (98 kpc) East-West field at 1.5 arcsec (1.3 kpc) resolution. (b) 53 arcsec (47 kpc) East-West field at 0.75 arcsec (0.66 kpc) resolution. (c) 22.5 arcsec (20 kpc) East-West field at 0.25 arcsec (0.22 kpc) resolution. (d) The jet/counter-jet intensity ratio for the inner (straight) section within 30 arcsec (26 kpc) of the nucleus at 0.75 arcsec (0.66 kpc) resolution. The labelled wedge indicates the grey-scale range. (e) A grey-scale of the total intensity with superposed polarization vectors, showing 30 arcsec from the nucleus of each jet at 0.75 arcsec (0.66 kpc) resolution. The superposed vectors indicate the degree of polarization p (on a scale given by the labelled bar) and the direction of the apparent magnetic field. (f) As in panel (e), but for the inner 5 arcsec of the main jet at 0.25 arcsec (0.22 kpc) resolution.

the main and counter-jet intensities at the same resolution. Panel (c) shows the jets at our highest resolution, 0.25 arcsec. The brightest region of the main jet is resolved into three knots embedded in more extended emission. The nucleus has an extension pointing in the direction of the main jet whose brightness drops rapidly with distance from the nucleus; it can only be seen out to ≈ 1 arcsec. No emission is visible at 0.25-arcsec resolution between this point and the first bright knot of emission ≈ 2 arcsec from the nucleus.

The polarization structure of B2 0326+39 is shown at resolutions of 0.50 and 0.25 arcsec in Figs 1(e) and (f), respectively. As is usual in FRI objects (Bridle & Perley 1984), the main jet close to the nucleus is polarized with an apparent field parallel to its axis. Further out in the main jet and in all parts of counter-jet with sufficient signal-to-noise ratio, the apparent field is perpendicular to the axis. In this object, unlike 3C 31 and B2 1553+24, no parallel field edge is seen.

We model the jets within 22 arcsec of the nucleus, where their ridge lines are straight.

2.5.2 B2 1553+24

Figs 2(a) – (c) show the jets of B2 1553+24 at three different resolutions: 1.5, 0.75 and 0.25 arcsec. The jets are very straight with only a slight bend in the main jet about 45 arcsec from the nucleus. Both jets get steadily fainter further out, and are lost in the noise approximately 65 and 45 arcsec from the nucleus for the main and counter-jets respectively in our lowest (1.5 arcsec) resolution image. The counter-jet is invisible within 3 arcsec of the nucleus; in contrast, the main jet is very bright there. Further out, the counter-jet brightens, reaching a maximum at 7 arcsec from the nucleus. From this point outwards, the main and counter-jets appear essentially identical, but with the main jet approximately twice as bright. This is also illustrated in the image of jet/counter-jet intensity ratio (Fig. 2d). Initially (within 1.5 arcsec) the main jet is well collimated, as are both jets at distances ≥ 7 arcsec. Both jets flare dramatically between these regions of good collimation.

The polarization structure of the jets in B2 1553+24 is shown in Figs 2(e) and (f) at resolutions of 0.75 and 0.25 arcsec respectively. The bright 4 arcsec of the main jet closest to the nucleus has an apparent magnetic field aligned along the jet axis. Further out, the field becomes perpendicular to the axis close to the centre of the jet and parallel to the outer isophotes near its edges.

We model the jets out to 30 arcsec from the nucleus. This limit is set not by changes in jet direction, as in 3C 31 and B2 0326+39, but by signal-to-noise, particularly in polarization.

3 THE MODEL

3.1 Assumptions

Our fundamental assumptions are those of LB:

- (i) The jets may be modelled as antiparallel, axisymmetric, stationary, laminar flows.
- (ii) They contain relativistic particles with an energy

spectrum $n(E)dE = n_0 E^{-(2\alpha+1)} dE$ (corresponding to a frequency spectral index α) with an isotropic pitch-angle distribution. The maximum degree of linear polarization is then $p_0 = (3\alpha + 3)/(3\alpha + 5)$. We assume that the 1.4 – 5 GHz spectral indices given in Sections 2.5.1 and 2.5.2 also apply at 8.4 GHz.

(iii) The magnetic field is tangled on small scales, but anisotropic (the reasons for taking the field to be of this form are discussed by Laing 1981, Begelman et al. 1984 and LB).

We define $\beta = v/c$, where v is the flow velocity. $\Gamma = (1 - \beta^2)^{-1/2}$ is the bulk Lorentz factor.

3.2 Overview

We aim to determine the velocity and angle to the line of sight independently by comparison of emission from the main and counter-jets and the modelling of linear polarization is essential to our technique. In order to illustrate this point, we consider the simple example of cylindrical, antiparallel jets with constant velocity βc at an angle θ to the line of sight. If we consider only total intensity, the ratio of the flux densities per unit length for the main and counter-jets, I_j/I_{cj} , does not uniquely determine the velocity:

$$\frac{I_j}{I_{cj}} = \left(\frac{1 + \beta \cos \theta}{1 - \beta \cos \theta} \right)^{2+\alpha}$$

for emission which is isotropic in the frame of the jet flow. In order to break the degeneracy between β and θ , we use the linear polarization. The relation between the angles to the line of sight in the rest frame of the flow, θ' and in the observed frame, θ , is:

$$\begin{aligned} \sin \theta'_j &= [\Gamma(1 - \beta \cos \theta)]^{-1} \sin \theta \quad (\text{main jet}) \\ \sin \theta'_{cj} &= [\Gamma(1 + \beta \cos \theta)]^{-1} \sin \theta \quad (\text{counter-jet}) \end{aligned}$$

The observed polarization is in general a function of θ' if the field is anisotropic. If we know the field structure a priori, then we can solve explicitly for β and θ . We take the example of a field which is disordered on small scales but confined to a plane perpendicular to the jet, with equal rms along any direction in the plane. In this case, there is no variation of the degree or direction of polarization across the jet. For $\alpha = 1$, the total and polarized flux densities per unit length in the emitted frame are:

$$\begin{aligned} I' &= K(1 + \cos^2 \theta') \\ P' &= p_0 K \sin^2 \theta' \end{aligned}$$

where K is a constant (Laing 1980, 1981). The ratios of observed total and polarized intensity for the jet and counter-jet are:

$$\begin{aligned} \frac{I_j}{I_{cj}} &= \left[\frac{2 - [\Gamma(1 - \beta \cos \theta)]^{-2} \sin^2 \theta}{2 - [\Gamma(1 + \beta \cos \theta)]^{-2} \sin^2 \theta} \right]^3 \\ \frac{P_j}{P_{cj}} &= \left(\frac{1 + \beta \cos \theta}{1 - \beta \cos \theta} \right)^5 \end{aligned}$$

These equations can be solved numerically for β and θ (cf. Bondi et al. 2000). [The specific field configuration is a reasonable approximation for the outer regions of the jets in B2 0326+39 (Section 5.2.4)].

In general, we must fit the field configuration and therefore need to introduce two additional parameters to describe its anisotropy (Section 3.5). These also determine the variation of polarization transverse to the jet axis, and can be estimated independently of the velocity and angle if the jets are well resolved in this direction.

Following LB, we model the jets using simple parameterized forms for the jet geometry, velocity, emissivity and magnetic-field structure. We find that the functional forms used by LB to model variations along the jets are unable to fit the new data. In order to produce models that fit the data accurately, we are forced to decouple the parameterizations of velocity, emissivity and magnetic field from the three regions defined by the geometry in LB. This provides much more freedom in our models, but also allows simpler functional forms to be used.

LB examined two forms for transverse variations of velocity and emissivity: *spine/shear-layer (SSL)* and *Gaussian*. The former gave a slightly better fit to the data for 3C 31, at the cost of introducing extra parameters. We find that the off-axis variations of velocity and emissivity are less well constrained in our objects and that the difference between SSL and Gaussian models is insignificant. In what follows, we use only the simpler Gaussian models.

3.3 Geometry & Coordinate Systems

The geometry of the model jet is sketched in Fig. 3. It is divided into two parts: a *flaring region* where the jet first expands rapidly and then recollimates and an *outer region* of constant opening angle. The mathematical description of the edge of the jet is as given by LB, but with two important changes. First, the conical outer region is not centred on the nucleus but at a distance A behind the nucleus along the jet axis, allowing the jet to recollimate much more than is seen in 3C 31 (Fig. 3). This modification is required to describe many FRI jets, including both B2 0326+39 and B2 1553+24. Second, we find no evidence for separate conical inner regions in the B2 sources (the jets are very narrow and poorly resolved close to the nuclei, so their collimation behaviour is poorly constrained there). We therefore extend the flaring region to the base of the jet. An inner region analogous to that used by LB to model 3C 31 is defined purely by the emissivity profile (Section 3.6). The distance of the outermost isophote from the jet axis in the flaring region is fit by a cubic polynomial, as in LB, but both it and its derivative are constrained to be zero at the nucleus ($\xi_1 = 0$ and $r_1 = 0$ in the notation of LB).

Four parameters define the geometry of the model. Of these, the angle to the line of sight, θ , the opening angle of the conical outer region, ξ_0 , and the distance along the axis from the nucleus to the boundary between flaring and outer regions, r_0 , are defined essentially as in LB. Because the vertex of the outer region is no longer at the nucleus, however, the spherical boundary surface is centred on the vertex and has radius $r_0 + A$ (this reduces to the case considered by LB if $A = 0$). The fourth defining parameter is x_0 , the radius of the jet edge at the outer boundary (Fig. 3). We

choose to optimize x_0 rather than A to avoid cross-coupling between variables: x_0 is determined by the position of the outer isophote at the boundary and ξ_0 by the expansion of the jet in the outer region, whereas A affects both quantities. The variables are related by $(r_0 + A) \sin \xi_0 = x_0$.

The velocity, emissivity and magnetic-field parameterizations defined below are expressed in a streamline coordinate system (ρ, s) where the streamline index s is constant for a given streamline and ρ increases monotonically with distance along it. The distance of a streamline from the jet axis is:

$$\begin{aligned} x(z, s) &= a_2(s)z^2 + a_3(s)z^3 & (\text{flaring region}) \\ x(z, s) &= (z + A) \tan(\xi_0 s) & (\text{outer region}) \end{aligned}$$

where z is the distance from the nucleus along the axis. In the outer region, $s = \xi/\xi_0$, where ξ is the angle between the flow vector and the jet axis. For the flaring region, $a_2(s)$ and $a_3(s)$ are defined by the conditions that $x(z, s)$ and its derivative with respect to z , $x'(z, s)$, are continuous at the boundary between the two regions. s therefore varies from 0 on-axis to 1 at the jet edge; the $s = 0.5$ streamline is plotted in Fig. 3. The form of $x(z, s)$ in the flaring region is that used by LB with the simplifying condition $x(0, s) = x'(0, s) = 0$. Parameterization of physical quantities in terms of the distance from the nucleus along a streamline creates undue complexity because of the cubic form of $x(z, s)$. Instead, we use a coordinate:

$$\begin{aligned} \rho &= \frac{z r_0}{(r_0 + A) \cos(\xi_0 s) - A} & \rho < r_0 \\ \rho &= \frac{z + A}{\cos(\xi_0 s)} - A & \rho \geq r_0 \end{aligned}$$

ρ increases monotonically along a streamline from 0 at the nucleus and each streamline crosses the boundary into the outer region at $\rho = r_0$. The coordinate system used by LB is the special case with $A = 0$.

3.4 Velocity field

The variations in sidedness ratio along the jets in both sources (Figs 1d, 2d) suggest that the initial velocity needs to be high in order to account for the asymmetry as a consequence of Doppler boosting. Further from the nucleus, there is a transition to a regime where the sidedness ratios are low and approximately uniform. In B2 1553+24, the ratio remains constant, but significantly >1 for all distances >7 arcsec from the nucleus, indicating a mildly relativistic but constant velocity. Two changes to the form of the velocity profile used by LB to describe 3C 31 are required:

- (i) In the flaring region, the function used by LB describes an initial fast section and abrupt deceleration, just as needed for the B2 sources, but the deceleration is forced to occur immediately before the jet recollimates. This does not appear to be general, so we need a functional form which is qualitatively similar to that used by LB, but which allows the location and length of the rapid deceleration region to be varied.
- (ii) The jet/counter-jet sidedness ratio in the outer region of 3C 31 continues to decline slowly with distance from the

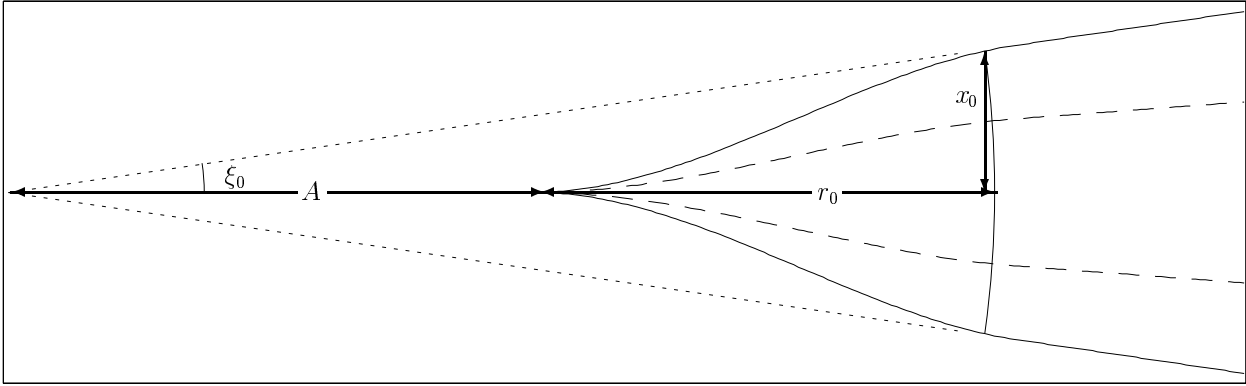


Figure 3. Geometry of the model. The jet edge ($s = 1$ streamline) is indicated by the solid line and the $s = 0.5$ streamline by the dashed line. The arc shows the spherical boundary between the flaring and outer regions, centred at the vertex of the outer region. The three quantities used to define the jet geometry: r_0 , the distance of the outer boundary from the nucleus; x_0 , the width of the jet at the outer boundary and ξ_0 , the opening angle of conical outer region are marked.

nucleus, so LB used an exponential form for the velocity profile there. This will not fit the large regions of constant sidedness ratio in the B2 sources, especially in B2 1553+24.

We therefore divide the on-axis velocity profile into three regions: (a) approximately constant, with a high velocity close to the nucleus; (b) a linear fall-off and (c) roughly constant, but with a low velocity at large distances. Example profiles are given later (Figs 16b and 18b). The profile is defined by four free parameters: the distances of the two boundaries separating the three regions, ρ_{β_1} and ρ_{β_0} , and the characteristic inner and outer velocities β_1 and β_0 .

The velocity along any off-axis streamline is calculated using the same expressions but with inner and outer velocities $\beta_1 \exp(-s^2 \ln v_1)$ and $\beta_0 \exp(-s^2 \ln v_0)$, respectively, i.e. with a truncated Gaussian transverse profile falling to fractional velocities v_1 and v_0 at the edge of the jet in the inner and outer regions, respectively. This differs slightly from the separable function used by LB, but gives essentially identical transverse profiles.

The full functional forms for the velocity field $\beta(\rho, s)$ are given in Table 4. [Note that the exponential terms are introduced purely to maintain continuity in the acceleration near the boundaries and their precise form has no significant effect on the brightness distribution]. The constants c_1 , c_2 , c_3 and c_4 are defined by the values of the free parameters and the conditions that the velocity and acceleration are continuous at the two boundaries.

3.5 Magnetic Field Structure

We define the rms components of the magnetic field to be $\langle B_l^2 \rangle^{1/2}$ (longitudinal, parallel to a streamline), $\langle B_r^2 \rangle^{1/2}$ (radial, orthogonal to the streamline and outwards from the jet axis) and $\langle B_t^2 \rangle^{1/2}$ (toroidal, orthogonal to the streamline in an azimuthal direction). The magnetic-field structure is parameterized, as in LB, by the ratio of rms radial/toroidal field, $j(\rho, s) = \langle B_r^2 \rangle^{1/2} / \langle B_t^2 \rangle^{1/2}$ and the longitudinal/toroidal ratio $k(\rho, s) = \langle B_l^2 \rangle^{1/2} / \langle B_t^2 \rangle^{1/2}$. The main difference between our model and that of LB is again that the characteristic distances are defined independently from those for other quantities. Two fiducial distances, ρ_{B_1} and ρ_{B_0} , are used. For $\rho < \rho_{B_1}$ and $\rho > \rho_{B_0}$, the field ratios have

constant values, with linear interpolation between them for $\rho_{B_1} \leq \rho \leq \rho_{B_0}$. We find no evidence for any transverse structure in either of the field ratios. In 3C 31, there are significant variations in the radial/toroidal field ratio between the centre and edge of the jet, and the model of LB is therefore more complex than that used here. The functional forms assumed for the field ratios are again given in Table 4.

3.6 Emissivity

We write the proper emissivity as $\epsilon(\rho, s)f(\rho, s)$, where ϵ is the emissivity in I for a magnetic field $B = \langle B_l^2 + B_r^2 + B_t^2 \rangle^{1/2}$ perpendicular to the line of sight. f depends on field geometry: for I , $0 \leq f \leq 1$ and for Q and U $-p_0 \leq f \leq +p_0$. Following LB, we refer to ϵ , loosely, as ‘the emissivity’. For a given spectral index, it is a function only of the rms total magnetic field and the normalizing constant of the particle energy distribution, $\epsilon \propto n_0 B^{1+\alpha}$.

The description of the emissivity is similar to that given by LB: the on-axis profile is divided into distinct regions, each with a power-law profile. As for the velocity, however, the boundaries between regions are defined without reference to the geometry. In order to differentiate between significant changes in the emissivity profile and small-scale, stochastic features (which will occur at different places in the main and counter-jets), we require evidence that the same emissivity structure is present in both jets and that it extends over many beam areas. Five regions are required (although only four are used for each source) compared with the three used by LB. The reasons for the increase in the number of regions are:

- (i) In B2 0326+39 the bright region of the main jet between 2 and 5 arcsec from the nucleus (Fig. 1b) is composed of three knots of emission of approximately equal brightness with a sharp falloff at each end; there is a much fainter equivalent in the counter-jet. Two regions are therefore required rather than the one used in LB: a relatively flat section averaging the intensity of the knots and a steep section modelling the rapid falloff at the end of the last knot. The rapid increase in brightness at the innermost knot is modelled using a discontinuity in the emissivity profile as in LB.
- (ii) A further region is required to model the outer parts

Table 4. Functional forms of the velocity β , emissivity ϵ , radial/toroidal and longitudinal/toroidal magnetic-field ratios j and k in the streamline coordinate system (ρ, s) . Column 4 lists the parameters which may be optimized, for comparison with Table 6.

Quantity	Functional form	Range	Free parameters
Velocity field			
$\beta(\rho, s)$	$\beta_1 - \left[\frac{\beta_1 \exp(-s^2 \ln v_1) - \beta_0 \exp(-s^2 \ln v_0)}{10} \right] \exp[c_1(\rho - \rho_{v_1})]$	$\rho < \rho_{v_1}$	Distances ρ_{v_1}, ρ_{v_0}
	$c_2 + c_3 \rho$	$\rho_{v_1} \leq \rho \leq \rho_{v_0}$	Velocities β_1, β_0
	$\beta_1 - \left[\frac{\beta_1 \exp(-s^2 \ln v_1) - \beta_0 \exp(-s^2 \ln v_0)}{10} \right] \exp[c_4(\rho_{v_0} - \rho)]$	$\rho > \rho_{v_0}$	Fractional edge velocities v_1, v_0
Emissivity			
$\epsilon(\rho, s)$	$g \left(\frac{\rho}{\rho_{e_1}} \right)^{-E_1}$	$\rho \leq \rho_{e_1}$	Distances $\rho_{e_1}, \rho_{e_2}, \rho_{e_3}, \rho_{e_4}$
	$\left(\frac{\rho}{\rho_{e_1}} \right)^{-E_2} \exp \left[-s^2 \ln \left(e_1 + (e_0 - e_1) \left(\frac{\rho - \rho_{e_1}}{\rho_{e_2} - \rho_{e_1}} \right) \right) \right]$	$\rho_{e_1} < \rho \leq \rho_{e_2}$	Indices E_1, E_2, E_3, E_4, E_5
	$d_1 \left(\frac{\rho}{\rho_{e_2}} \right)^{-E_3} \exp(-s^2 \ln e_0)$	$\rho_{e_2} < \rho \leq \rho_{e_3}$	Fractional increase g
	$d_2 \left(\frac{\rho}{\rho_{e_3}} \right)^{-E_4} \exp(-s^2 \ln e_0)$	$\rho_{e_3} < \rho \leq \rho_{e_4}$	
	$d_3 \left(\frac{\rho}{\rho_{e_4}} \right)^{-E_5} \exp(-s^2 \ln e_0)$	$\rho > \rho_{e_4}$	
Radial/toroidal field ratio			
$j(\rho, s)$	j_1	$\rho \leq \rho_{B_1}$	Distances ρ_{B_1}, ρ_{B_0}
	$j_1 + (j_0 - j_1) \left(\frac{\rho - \rho_{B_1}}{\rho_{B_0} - \rho_{B_1}} \right)$	$\rho_{B_1} < \rho < \rho_{B_0}$	Ratios j_1, j_0
	j_0	$\rho \geq \rho_{B_0}$	
Longitudinal/toroidal field ratio			
$k(\rho, s)$	k_1	$\rho \leq \rho_{B_1}$	Ratios k_1, k_0
	$k_1 + (k_0 - k_1) \left(\frac{\rho - \rho_{B_1}}{\rho_{B_0} - \rho_{B_1}} \right)$	$\rho_{B_1} < \rho < \rho_{B_0}$	
	k_0	$\rho \geq \rho_{B_0}$	

of both jets in B2 1553+24 (we will show that this is on a much larger physical scale than the entire modelled regions of 3C 31 and B2 0326+39; it is therefore reasonable that it shows different emissivity behaviour).

The emissivity is continuous across all of the boundaries except the innermost ($\rho = \rho_{e_1}$), where a jump by a factor of g is allowed. The part of the jet with $\rho < \rho_{e_1}$ is analogous to

the inner region defined by geometry, emissivity and velocity for 3C 31 (LB).

Off-axis, the profile is multiplied by a factor $\exp[-s^2 \ln \bar{e}(\rho)]$, as in LB, so that $\bar{e}(\rho)$ is the fractional value of the emissivity at the jet edge. $\bar{e}(\rho)$ has a constant value e_0 for $\rho > \rho_{e_2}$ and varies linearly through region 2 from e_1 at ρ_{e_1} to e_0 at ρ_{e_2} . In the inner region the jet is too narrow to constrain any transverse profile and we set $\bar{e}(\rho) = 1$.

Table 5. The number of independent points and the reduced χ^2 values for our final optimized models.

Object	Independent points	Reduced χ^2
B2 0326+39	3614	1.32
B2 1553+24	3722	1.13

The full description of the emissivity distribution $\epsilon(\rho, s)$ is given in Table 4.

3.7 Modelling Procedure

The modelling procedure is that described by LB, with one small refinement. In order for the numerical integrations to converge, it is necessary to determine appropriate limits, which are where the line of sight intersects the jet surface. If θ is small, a line of sight may cross the jet boundary more than twice, for example in passing through both the inner part of the jet and the shoulder where the jet recollimates. This possibility is required for B2 1553+24 and is now included.

3.8 Fitting and optimization

We use χ^2 as a measure the goodness of fit. The noise level for each resolution and Stokes parameter is estimated as $1/\sqrt{2}$ times the rms difference between the image and a copy of itself reflected across the jet axis, as in LB. This quantity is always significantly larger than the off-source noise level. It is a measure of the local deviation from mirror symmetry, which limits our ability to fit the data using an axisymmetric model, and includes a contribution from any residual deconvolution errors. It is a lower limit to the correct noise level, as it excludes any mirror-symmetric component. We therefore expect χ^2 to be *overestimated*.

χ^2 is calculated using the high-resolution (0.25 arcsec) images where they have adequate signal-to-noise ratio (i.e. close to the nucleus) and the lower-resolution images elsewhere. χ^2 values for I , Q and U are summed. In a slight modification to the algorithm used by LB, the sizes of the regions over which χ^2 is evaluated from the high-resolution data may be different for total intensity and linear polarization. For B2 0326+39 we fit to the 0.25-arcsec I within 4.5 arcsec, further out, we use the 0.5-arcsec image; for the Q and U images only the 0.5-arcsec images are used. For B2 1553+24 we fit the inner 4 arcsec of the 0.25-arcsec I , Q and U images and the 0.75-arcsec images at larger distances. The sampling grid is chosen so that all estimates of χ^2 are independent and the core is always excluded.

An initial starting model is generated by adjusting a number of key parameters by hand to match recognizable features of the jet. Their values are then fixed and the remaining parameters are optimized using the downhill simplex method of Nelder & Mead implemented using Numerical Recipes routines (Press et al. 1992) to minimize χ^2 .

3.9 Uniqueness and errors in parameter estimation

The uniqueness of such a complex model is a concern, especially given that the downhill simplex algorithm is not guaranteed to converge to a global χ^2 minimum. In addition, the parameters are clearly not independent, and coupling between them leads to some indeterminacy. We are confident of the reliability of our models, however, for the following reasons:

- (i) We fit to deep, well-resolved images in I , Q and U . These provide a large number of independent data points with good signal-to-noise ratio.
- (ii) We have experimented with a wide range of starting conditions and have been unable to find satisfactory solutions which differ significantly from those presented here: models even remotely resembling the data are hard to find.
- (iii) Whilst changes in some parameters can, in part, be offset by the variation of others, the extent to which this can occur is strictly limited by the fact that most parameters only affect the fit in limited regions and are well constrained by gross features in the brightness distributions.

We derive rough uncertainties, as in LB, by varying individual parameters until the increase in χ^2 for total intensity or linear polarization in either the flaring or the outer region corresponds to the formal 99% confidence level for independent Gaussian errors. These estimates are crude (they neglect coupling between parameters), but in practice give a good representation of the range of qualitatively reasonable models.

4 COMPARISON BETWEEN MODELS AND DATA

4.1 χ^2 values

The values of reduced χ^2 for the final optimized models of the two sources are listed in Table 5. Given that the “noise levels” are probably underestimated (Section 3.8), these represent very good fits. In the remainder of this section, we compare the models and data in detail.

4.2 B2 0326+39

4.2.1 Total intensity images and profiles

Figs 4 and 5 show model and observed contour plots and profiles along the jet axis for Stokes I at 0.50 and 0.25 arcsec resolution, respectively. The model and observed sidedness ratios are shown as grey-scale plots and on-axis profiles in Fig. 6.

4.2.2 Fitted total intensity features

Our optimized model successfully reproduces the following features of the total-intensity distribution in B2 0326+39, as illustrated in Figs 4 – 6:

- (i) The base of the main jet is initially bright but fades rapidly away from the nucleus and becomes invisible after 1 arcsec.

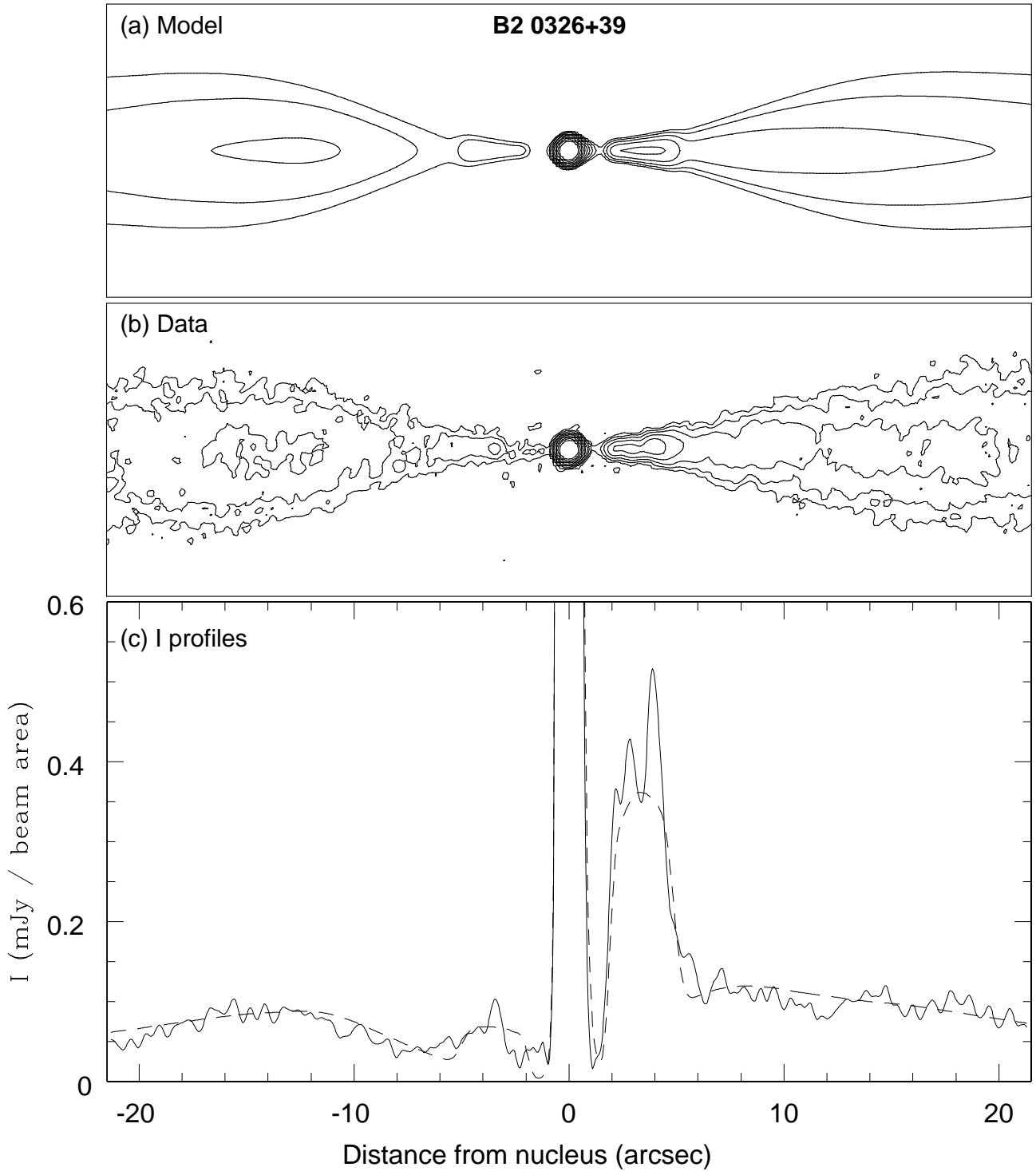


Figure 4. A comparison of the model and data for B20326+39 in total intensity at 0.50 arcsec resolution for the inner 21 arcsec of each jet. (a) model contours; (b) observed contours. The contour levels in panels (a) and (b) are 1, 2, 4, 8, 16, 32, 64, 128, 256, $512 \times 20 \mu\text{Jy}/\text{beam area}$. (c) Profiles along the jet axis for the data (solid line) and model (dashed line).

(ii) Apart from the bright base of the main jet, both jets are very faint within 2 arcsec of the nucleus.

(iii) The main jet has a very bright section between 2 and 4.5 arcsec from the nucleus, brightening and fading very quickly at each end.

(iv) A similar, but much fainter, peak in the brightness of the counter-jet is also reproduced.

(v) The main jet beyond 5 arcsec has a very flat profile, in contrast to the counter-jet which peaks at ≈ 15 arcsec from the nucleus.

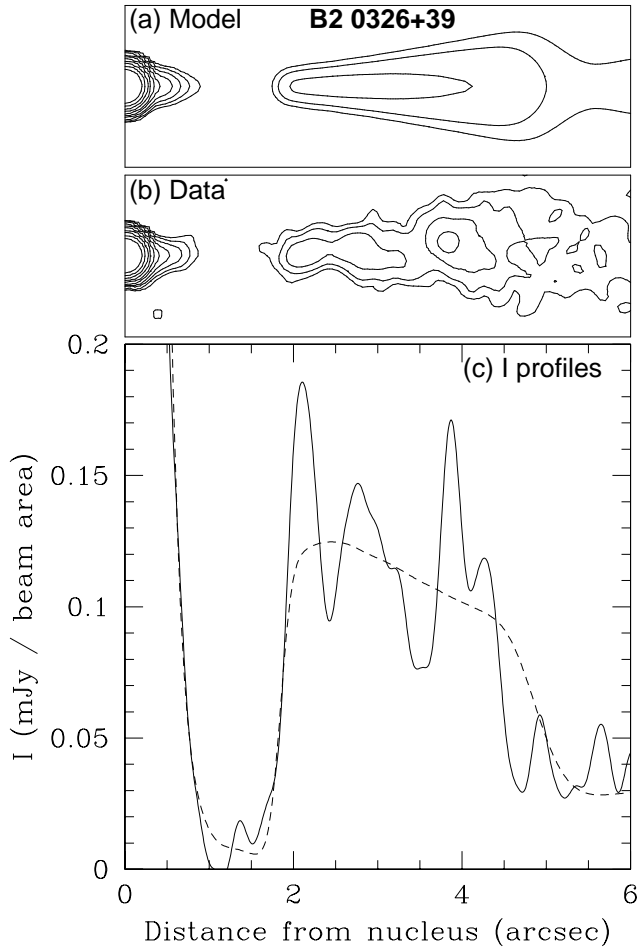


Figure 5. A comparison of the model and data in total intensity at 0.25 arcsec resolution for the inner 6 arcsec of the main jet in B2 0326+39. (a) model contours; (b) observed contours. The levels in panels (a) and (b) are 1, 2, 4, 8, 16, 32, 64, 128, 256, $512 \times 25 \mu\text{Jy}/\text{beam area}$. (c) Profiles along the jet ridge-line for the data (solid line) and model (dashed line).

(vi) The jets are initially well collimated, flare 5 arcsec from the nucleus and recollimate at ≈ 15 arcsec.

(vii) The on-axis sidedness ratio falls over the first half of the modelled region to near unity at 11 arcsec. This value is maintained over the outer 10 arcsec.

4.2.3 Polarization images and profiles

Fig. 7 illustrates the observed and model polarization structures of the jets in B2 0326+39 as grey-scales of the degree of polarization, p , vector plots representing p and the apparent magnetic field direction and profiles of p along the jet centre-line. There is little transverse variation of the degree or direction of polarization across the jets at large z (Figs 7b and d) and the ridge-line profiles are quite noisy, so we also show profiles of p averaged across the jets from 10 – 21.5 arcsec from the nucleus in Fig. 8. Vector plots for the inner regions of the main jet are shown on an expanded scale in Fig. 9. The 0.25 arcsec resolution images have low polarized signal-to-noise ratio and are not shown.

Individual transverse profiles of p are also noisy, so Fig. 10 shows averages over the outer parts of the main and

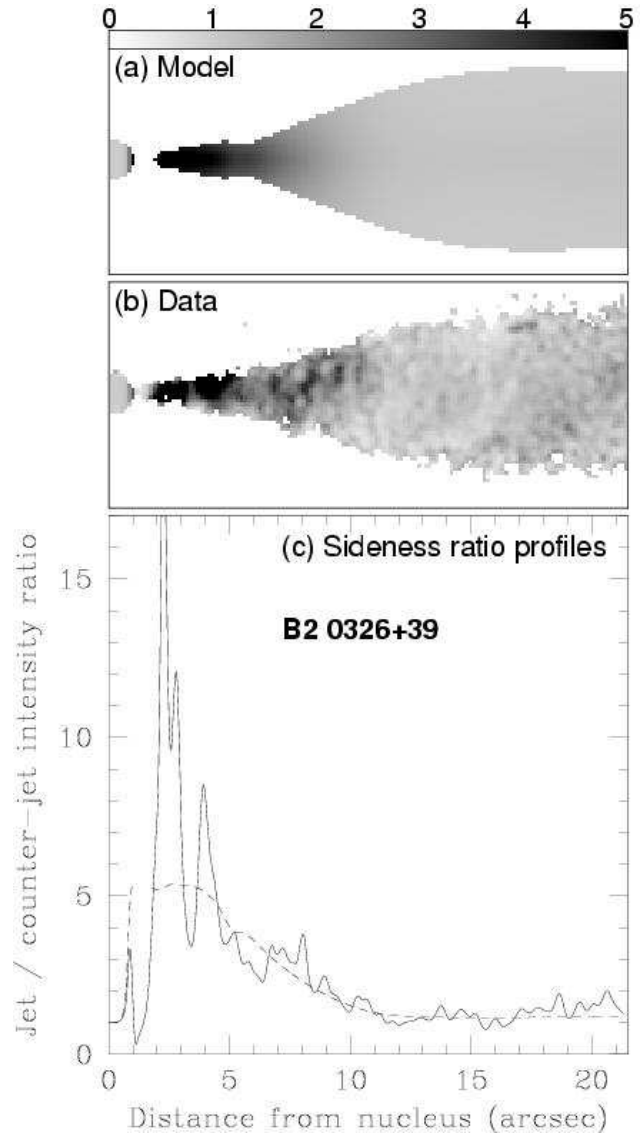


Figure 6. A comparison of the model and observed jet/counter-jet sidedness ratios at 0.50 arcsec for B2 0326+29. (a) Model grey-scale; (b) observed grey-scale. The grey-scale range for panels (a) and (b) is 0 – 5, as indicated by the labelled bar. (c) Profiles along the jet ridge-line for the data (solid line) and model (dashed line).

counter-jets (between 15 and 21 arcsec from the nucleus), where there is little longitudinal variation.

4.2.4 Fitted polarization features

Our model is successfully able to reproduce the following features in the polarization images (Figs 7–10):

(i) The inner knot and the bright regions of the main jet within 5 arcsec of the nucleus have longitudinal apparent magnetic field.

(ii) The bright part of the main jet is more polarized at its edges, forming a V-shaped structure in p (Figs 7a and b).

(iii) In this region, the on-axis degree of polarization falls

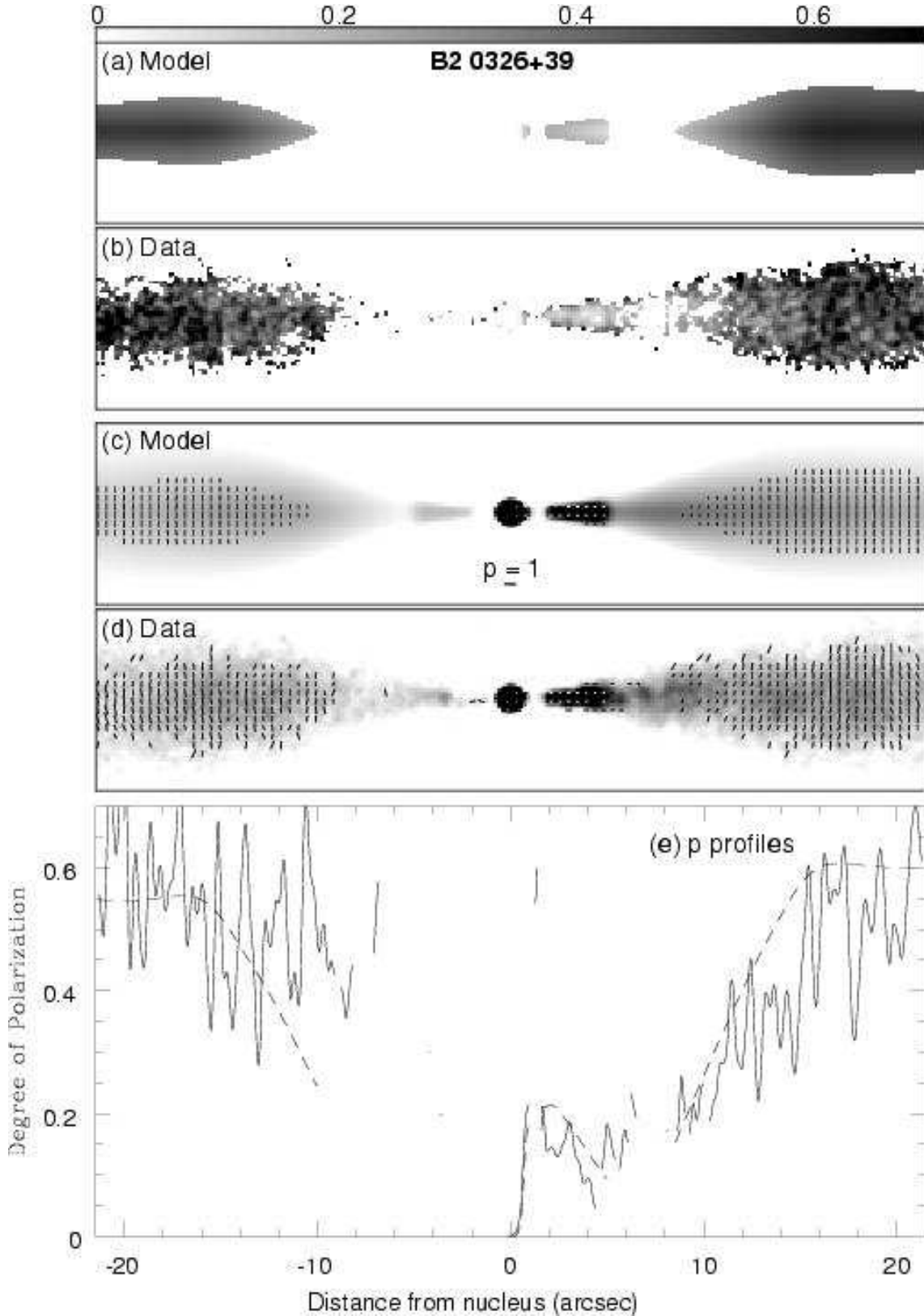


Figure 7. A comparison of the model and observed polarization distributions at 0.50 arcsec resolution in the inner ± 21 arcsec of the jets in B2 0326+39. (a) and (b): grey-scales of the degree of polarization, p . The grey level is indicated by the labelled bar at the top of the figure. (a) model; (b) data. (c) and (d): vector plots showing the degree and direction of linear polarization superimposed on grey-scales of total intensity. The lengths of the vectors are proportional to p (on a scale given by the labelled bar in panel c) and their directions are those of the apparent magnetic field. (c) model; (d) data. (e) Profiles of degree of polarization along the centre-line of the jet for the data (solid line) and model (dashed line). In all displays, the data and models have been blanked wherever the polarized power is $< 3\sigma_p$ or the total intensity is $< 5\sigma_I$, using the values of off-source noise given in Table 2.

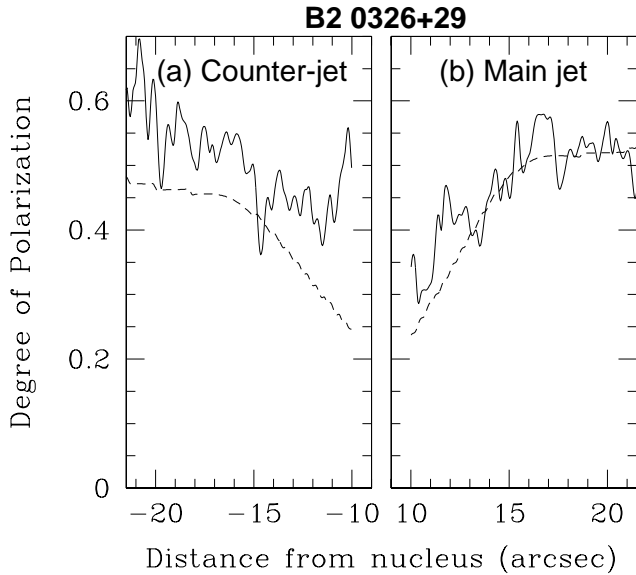


Figure 8. Profiles of the degree of polarization averaged across the jets of B20326+39. Full line: data; dashed line: model. The plots cover the range 10 – 21.5 arcsec from the nucleus, where there is little variation across the jets (Fig. 10). (a) counter-jet; (b) main jet. The resolution is 0.5 arcsec FWHM.

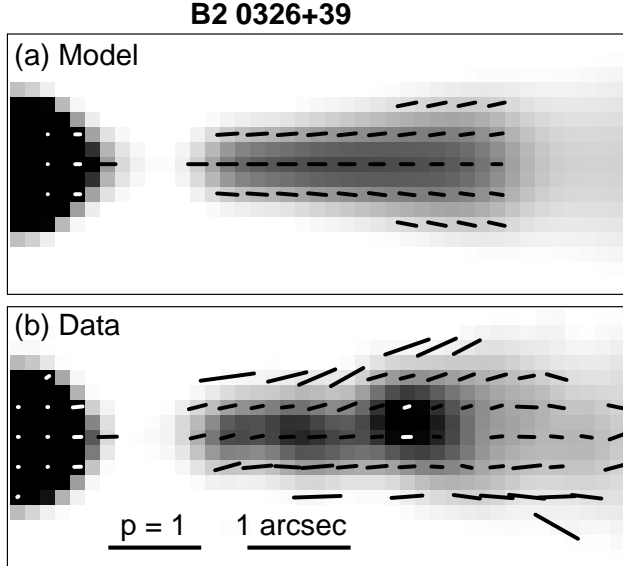


Figure 9. Vector plots of the degree and direction of linear polarization superimposed on grey-scales of total intensity for the inner 6 arcsec of the main jet in B20326+39 at a resolution of 0.50 arcsec. The vector lengths are proportional to the degree of polarization, p and their directions are those of the apparent magnetic field. (a) model; (b) data.

from 0.2 at the base of the main jet to 0.1 at 4 arcsec (Fig. 7c).

(iv) The main jet has a region where no polarized signal is detected at the 3σ level between 5 and 9 arcsec, setting a limit of $p < 0.15$. The model distribution is consistent with this limit. In the counter-jet, no significant polarized signal is seen closer than 10 arcsec from the nucleus and none is

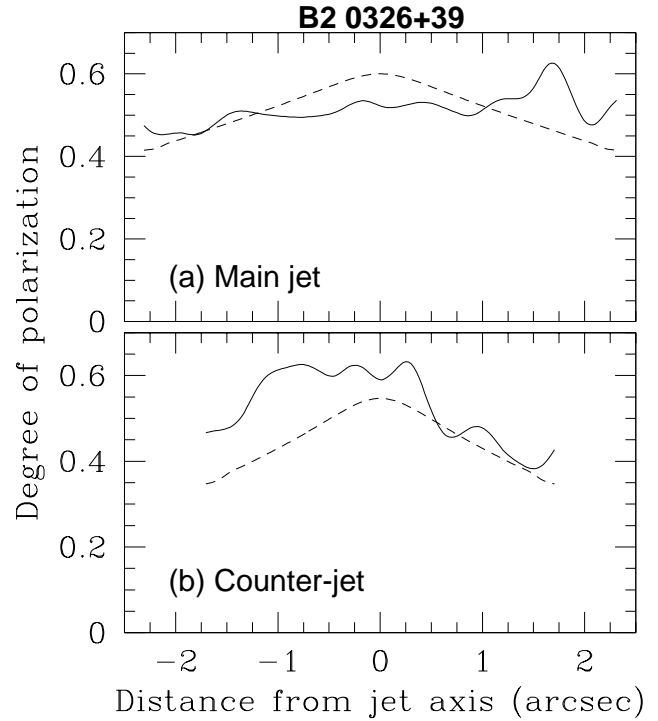


Figure 10. Transverse profiles of the degree of polarization in B20326+39 obtained by averaging over z between 15 and 21 arcsec. Full line: data; dashed line: model. The observed profiles are derived by averaging over images of p made without blanking, in order to avoid biasing the results to high values. The resolution is 0.5 arcsec FWHM.

predicted (the observational limits are not severe because of the low total intensity).

(v) Beyond 10 arcsec from the nucleus, the jet is polarized such that the apparent magnetic field vector is transverse to the jet axis and no parallel-field edge is seen.

(vi) Between 10 and 15 arcsec, the polarizations of both the jet and counter-jet increase monotonically before becoming constant with $p \approx 0.5$ further out. [The apparent underestimation of p in the counter-jet at ≈ 10 arcsec from the nucleus is in a region of low polarized signal and is probably not significant].

4.2.5 Features that cannot be fitted well

Our model cannot reproduce small-scale and/or non-axisymmetric features, the most prominent of which are the three knots of emission in the bright region of the main jet between 2 and 4.5 arcsec from the nucleus (Fig 5). The model correctly averages the brightness in this region into a smooth profile. In addition, there are a number of small, but significant discrepancies between model and data:

(i) The inner region of the counter-jet is observed to be brighter than that of the main jet (Fig 4b), an effect that is impossible to reproduce using intrinsically identical jets. This may also be caused by fluctuations on a small scale (e.g. a single knot in the counter-jet).

(ii) The counter-jet first brightens significantly 1 arcsec further from the nucleus than the main jet and the minimum in the total intensity profile at the end of the flaring region is

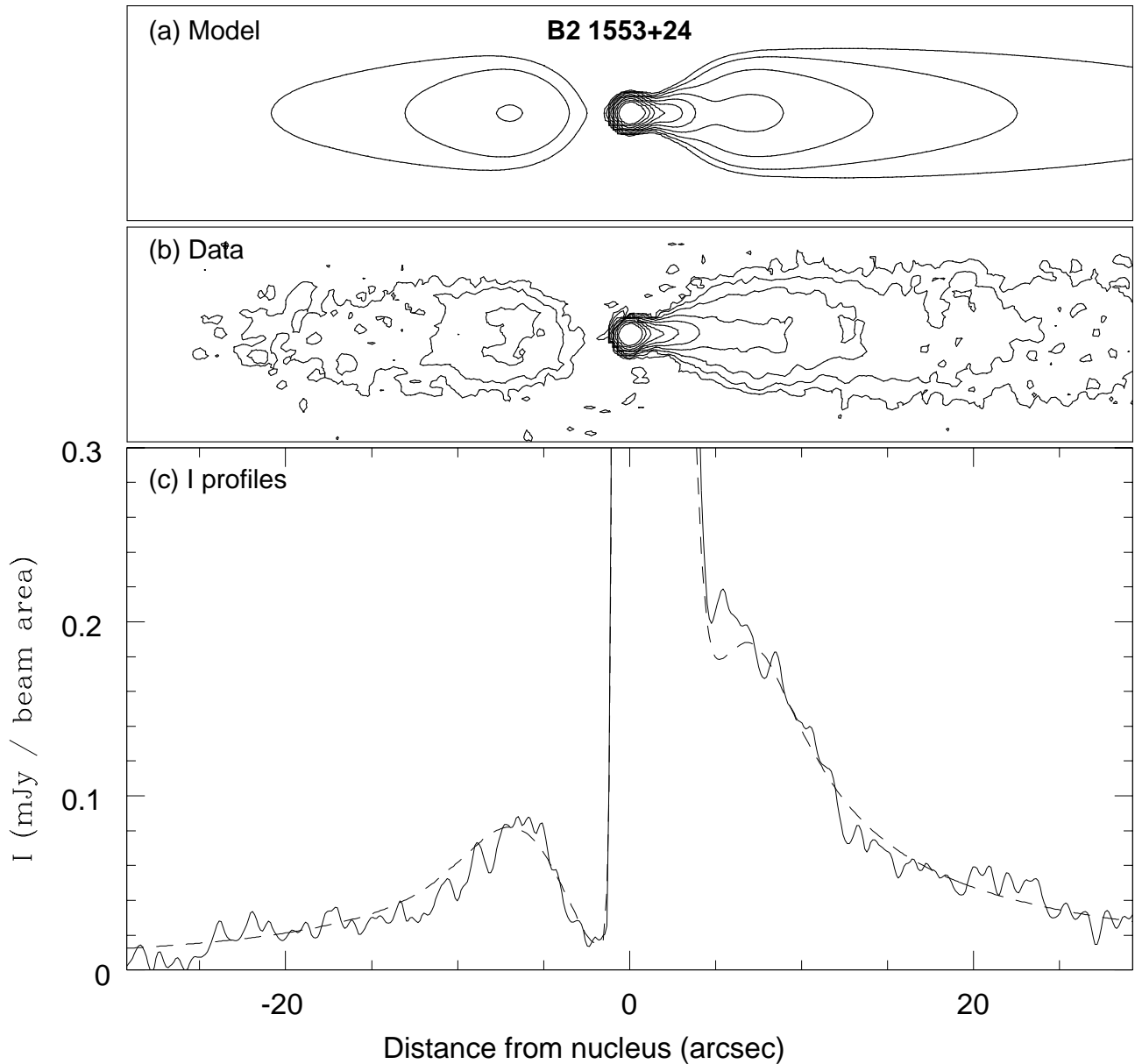


Figure 11. A comparison of the model and observed total intensity for B2 1553+24 at 0.75 arcsec resolution. The plots show the inner ± 29 arcsec. (a) and (b): contour plots of total intensity with levels at 1, 2, 4, 8, 16, 32, 64, 128, 256, $512 \times 20 \mu\text{Jy}/\text{beam area}$. (a) model; (b) data. (c) Profiles along the jet centre-line for the data (solid line) and model (dashed line).

2 arcsec further from the nucleus in the counter-jet (Fig 4c). This is not reproducible by our model, for which the overall shape of the flaring region should be similar for the two jets, even if their brightnesses differ significantly.

(iii) The counter-jet intensity decreases with z faster than the model predicts for $z > 15$ arcsec. This has the effect of increasing the sidedness ratio slightly in this region, an effect which is inconsistent with a monotonically decelerating flow (see Section 6.2).

(iv) The model predicts a degree of polarization which is slightly higher for the main jet than the counter-jet at large z . The converse is true, although the discrepancy is marginal (Figs 7e and 8).

(v) In the outer parts of the modelled region, p is predicted to be higher on-axis than at the jet edges. This is

marginally inconsistent with the data for the main jet, where p has little if any transverse variation (Fig. 10).

4.3 B2 1553+24

4.3.1 Total intensity images and profiles

Figs 11 shows contours and longitudinal profiles of total intensity for the model and observed images at 0.75 arcsec resolution. Corresponding plots for the inner 5 arcsec of the main jet at 0.25-arcsec resolution are shown in Fig. 12 (the counter-jet is invisible close to the nucleus on these images). The model and observed sidedness ratios are compared in Fig. 13.

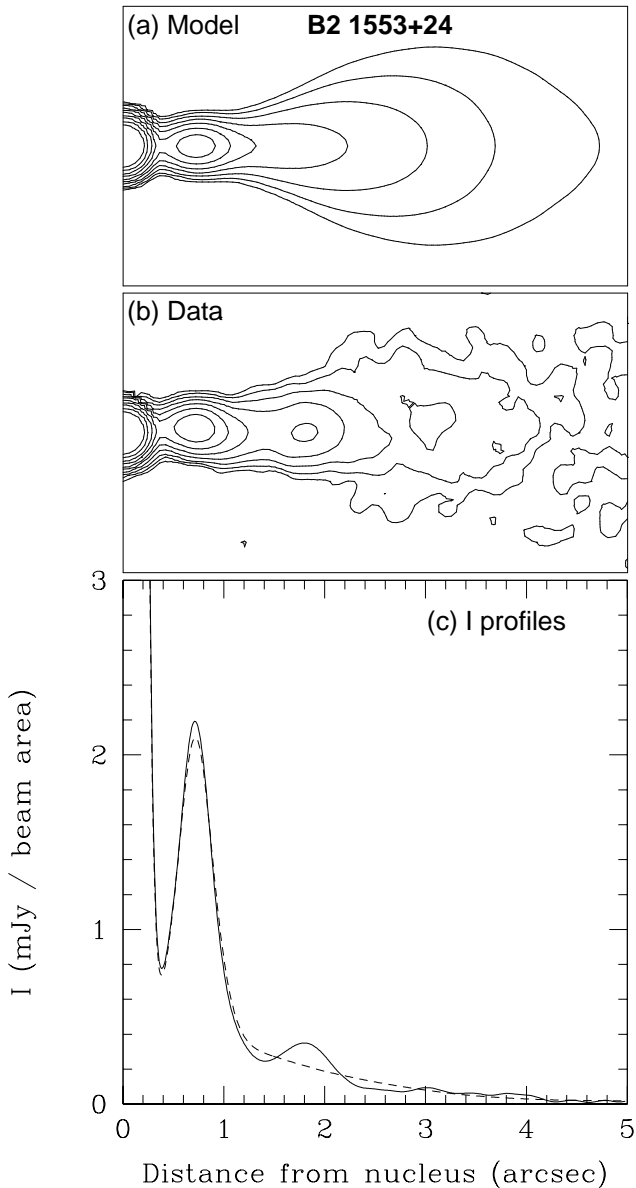


Figure 12. A comparison of the model and observed total intensity at 0.25 arcsec resolution for the inner 5 arcsec of the main jet in B2 1553+24. (a) and (b): contour plots with levels at 1, 2, 4, 8, 16, 32, 64, 128, 256, $512 \times 20 \mu\text{Jy}/\text{beam area}$. (a) model; (b) data. (c) A profile along the jet centre-line showing the observed (solid line) and model (dashed line) values.

4.3.2 Fitted total intensity features

The following features of the jets in B2 1553+24 are fitted accurately by our optimized model:

- (i) The main jet initially brightens very rapidly away from the nucleus, peaking at 0.7 arcsec separation and then fading to give the appearance of a bright knot.
- (ii) This jet remains well-collimated for 1.5 arcsec before flaring abruptly.
- (iii) At $z \approx 7$ arcsec, both jets recollimate, maintaining an approximately constant width at large z .
- (iv) The counter-jet is not seen in the inner 3 arcsec of the

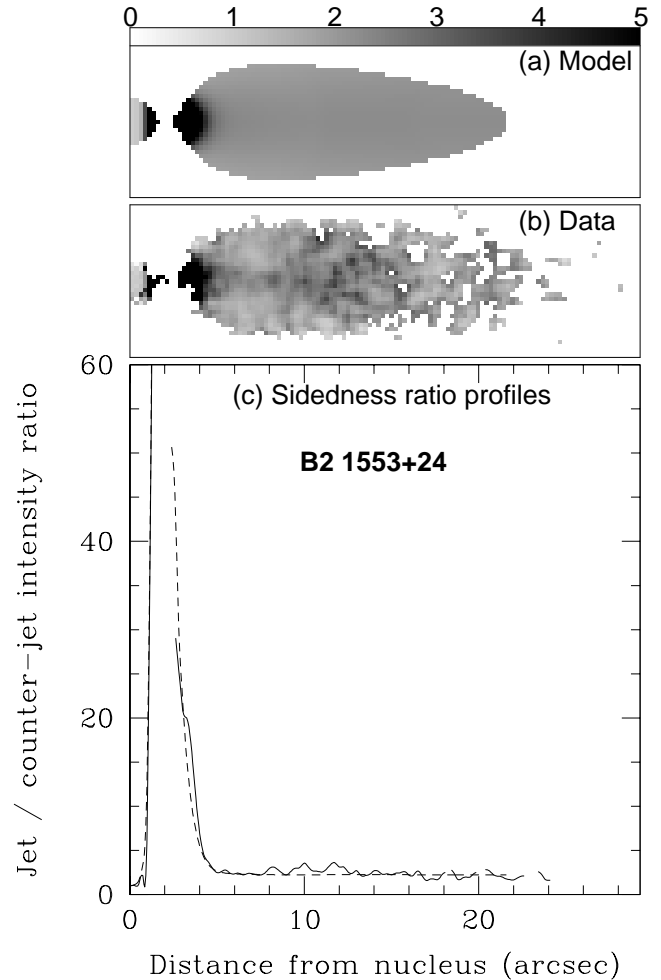


Figure 13. A comparison of the model and observed jet/counter-jet sidedness ratios at 0.75 arcsec for B2 1553+24. (a) and (b): grey-scale images of sidedness ratio, in the range 0 – 5 as indicated by the labelled bar. (a) model; (b) data. (c) sidedness profiles along the centre-line of the jet showing data (full line) and model (dashed line).

0.75-arcsec resolution image. After this point it brightens, reaching a peak ≈ 7 arcsec from the nucleus.

(v) At $z \approx 6$ arcsec in the main jet, the total intensity profile flattens before falling again from $z \approx 8$ arcsec.

(vi) The jet/counter-jet sidedness ratio drops rapidly with z , reaching a constant value of ≈ 2.2 at $z \approx 6$ arcsec.

4.3.3 Polarization images and profiles

Fig 14 shows grey-scale images of the degree of polarization p and vector images showing the orientation of the apparent magnetic field at both 0.75 and 0.25 arcsec resolution, together with profiles of p along the jet axis. Transverse profiles of the degree of polarization at two representative points in the jet and one in the counter-jet are shown in Fig 15.

4.3.4 Fitted polarization features

Our model is successfully able to reproduce the following features of the linear polarization in B2 1553+24:

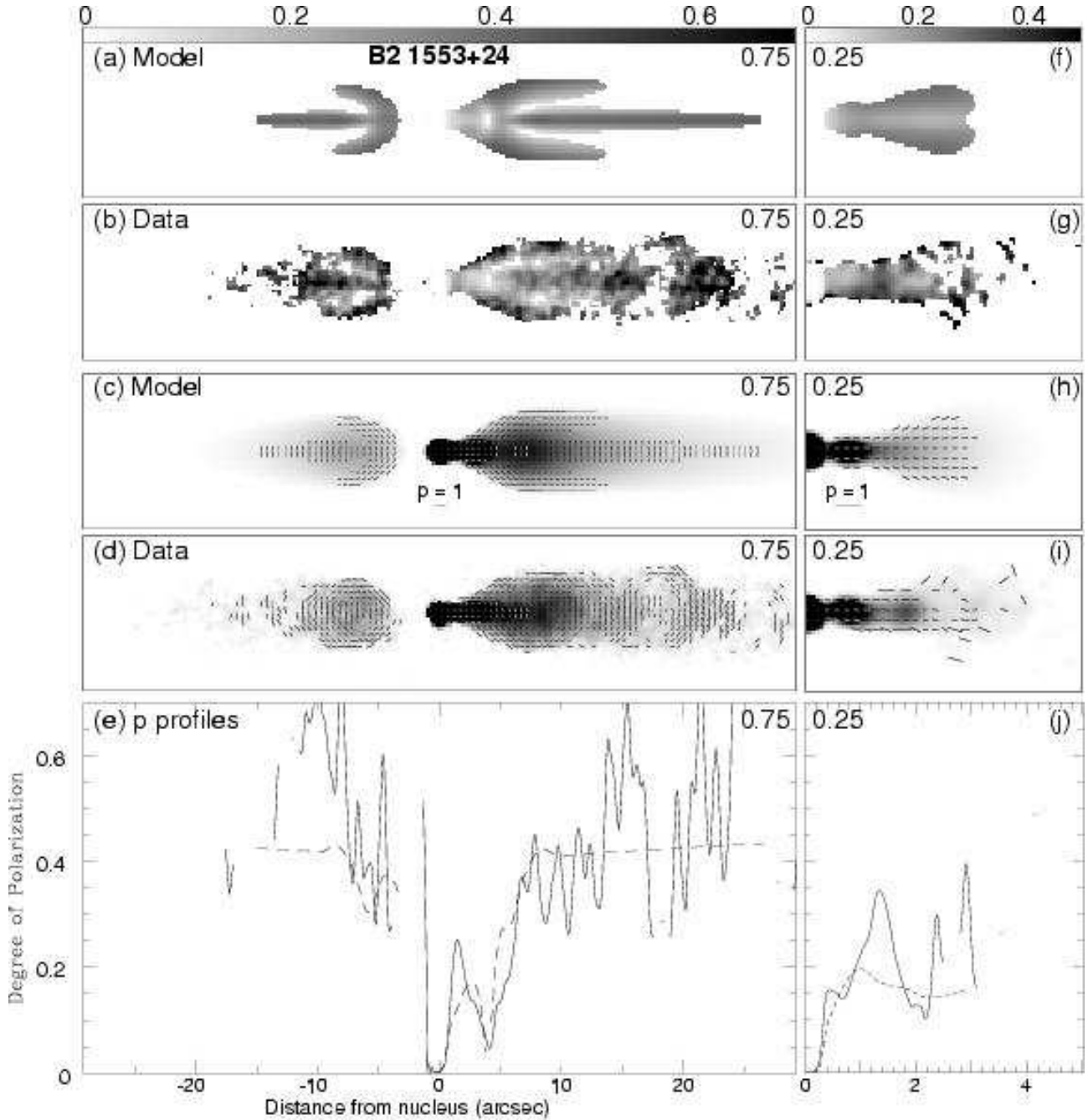


Figure 14. A comparison of the model and observed polarization for B2 1553+24. Panels (a) – (e) show the inner ± 29 arcsec at 0.75 arcsec resolution. (a) and (b): grey-scale images of the degree of polarization, p , in the range 0 – 0.7, as indicated by the labelled wedge. (a) model; (b) data. Panels (c) and (d) are vector plots showing the degree of polarization and the apparent magnetic field direction. The vector lengths are proportional to p , on a scale indicated by the bar on panel (c). (c) model; (d) data. (e) Profiles of the degree of polarization along the centre-line of the jet for model (dashed) and data (full). The data and models have been blanked wherever the polarized signal is $< 3\sigma_P$ or the total intensity is $< 5\sigma_I$, using the values of off-source noise as given in Table 2. Panels (f) – (j): as (a) – (e), but for the inner 5 arcsec of the main jet at a resolution of 0.25 arcsec. Note that the grey-scale range in panels (f) and (g) is 0 – 0.5 and therefore differs from that in panels (a) and (b).

(i) Within 3.5 arcsec of the nucleus, the degree of polarization is approximately constant on-axis, with $p \approx 0.15$. It increases with distance from the axis, reaching ≈ 0.3 at the edge of the jet.

(ii) In this region the apparent field is orientated approximately parallel to the jet axis.

(iii) At ≈ 4 arcsec from the nucleus the polarization on-axis in the main jet is very low.

(iv) Between 4 and 8 arcsec from the nucleus the on-axis polarization in the main jet increases to $p \approx 0.4$; further out it remains approximately constant at that value.

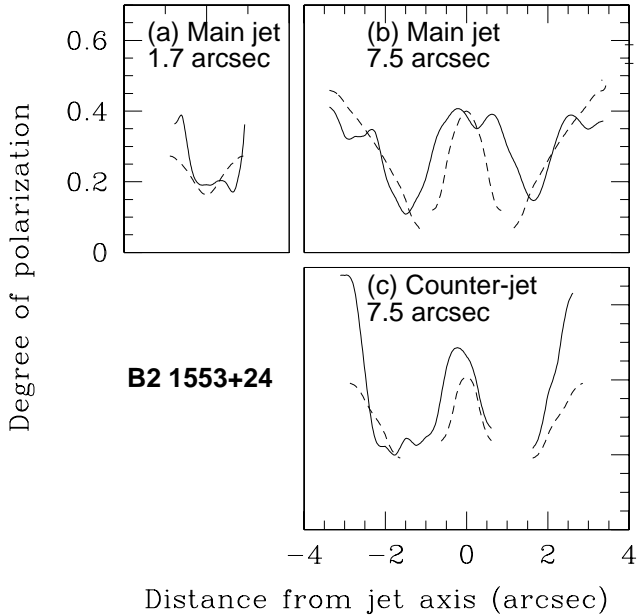


Figure 15. Transverse profiles of the degree of polarization in B2 1553+24. (a) Profile at a distance of 1.7 arcsec from the nucleus in the main jet. The apparent field is parallel to the jet axis across the entire width. (b) and (c) Profiles at 7.5 arcsec from the nucleus for the main and counter-jets, respectively. In both jets, the apparent field is parallel to the jet axis near the jet edge and perpendicular towards the centre. Full line: data; dashed line: model. The profiles are blanked as in Fig. 14 and the resolution is 0.75 arcsec.

(v) The counter-jet polarization on-axis remains approximately constant where it can be measured (4 - 15 arcsec)

(vi) Further than 4 arcsec from the nucleus, both the jet and counter-jet are polarized with a transverse apparent field on-axis.

(vii) The apparent field is longitudinal along the edges of both jets wherever there is significant signal.

(viii) There is a semicircular arc of enhanced polarized emission with a circumferential apparent field in the counter-jet, between 4 and 8 arcsec from the nucleus.

4.3.5 Features that cannot be fitted well

Our model cannot fit the following features:

(i) The bright knot at the base of the main jet does not lie exactly on the jet axis and cannot be fitted precisely by our axisymmetric model.

(ii) There is a second knot 1.9 arcsec from the nucleus, where the jet starts to expand rapidly (Fig. 12b and c). It would be possible to fit this feature by adjusting the emissivity profile to be much flatter locally, in which case the increase in path length through the jet would naturally generate a maximum. In the absence of any constraint from the counter-jet, this complication cannot be justified.

(iii) The arc of emission ≈ 20 arcsec from the nucleus in the main jet, particularly noticeable in the polarized images, and similar to a prominent feature seen in 3C31 (LB), cannot be fitted.

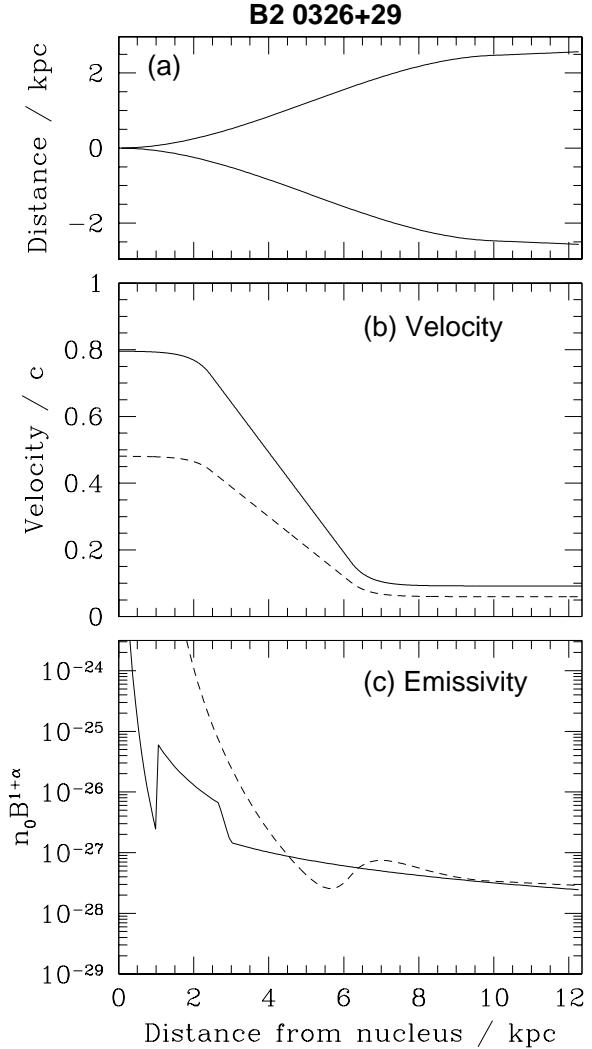


Figure 16. Profiles of intrinsic parameters along the jets of B2 0326+39 as functions of z (not projected on the sky). (a) the shape of the jet edge (the scales are the same for both axes). (b) the velocity profile along the jet axis (solid line) and jet edge (dashed line). (c) the on-axis emissivity profile, converted to $n_0 B^{1+\alpha}$ with n_0 in m^{-3} and B in T. Solid line: model; dashed line: adiabatic approximation with the magnetic-field evolution expected from flux freezing. The normalization for the adiabatic profile is set so that it agrees with the free model at large distances from the nucleus.

5 PHYSICAL PARAMETERS

5.1 Model parameters and confidence limits

The following section examines the structures of the jets implied by our models. All distances from the nucleus are given in linear units in the jet frame (i.e. *not* in projection on the sky).

Table 6 gives the fitted parameters and error estimates, defined as in Section 3, for both sources.

Table 6. Fitted parameters and error estimates.

Quantity	Symbol	0326+39			1553+24		
		opt	min ^a	max ^b	opt	min	max
Angle to line of sight (degrees)	θ	63.8	59.0	68.9	7.7	6.5	9.0
Geometry							
Boundary position (kpc)	r_0	10.02	9.52	10.60	48.15	44.56	51.57
Jet half-opening angle (degrees)	ξ_0	2.37	<	6.75	0.75	0.53	1.32
Width of jet at outer boundary (kpc)	x_0	2.47	2.28	2.64	3.36	3.09	3.75
Velocity							
Boundary positions (kpc)							
inner	ρ_{v_1}	2.43	0.68	4.10	21.01	10.78	25.71
outer	ρ_{v_0}	6.17	4.88	7.53	28.04	17.69	36.38
On – axis velocities / c							
inner	β_1	0.80	0.64	0.93	0.74	0.70	> ^c
outer	β_0	0.09	<	0.18	0.17	0.13	0.21
Fractional velocity at edge of jet							
inner	v_1	0.60	0.28	1.01	0.83	0.68	0.95
outer	v_0	0.65	<	4.34	0.63	0.23	> ^c
Emissivity							
Boundary positions (kpc)							
inner	ρ_{e_1}	1.05	0.73	1.19	0.00		
2	ρ_{e_2}	2.68	2.62	2.77	4.87	4.66	5.09
3	ρ_{e_3}	3.00	2.93	3.05	7.58	7.23	7.89
4	ρ_{e_4}		not used		23.13	20.27	26.02
On – axis emissivity exponents							
inner	E_1	6.08	5.03	6.41			
2	E_2	2.39	1.52	2.83	0.00	0.00	0.88
3	E_3	12.15	10.66	15.09	8.38	7.81	8.85
4	E_4	1.27	1.08	1.43	3.34	3.15	3.52
5	E_5				1.87	1.72	2.04
Fractional emissivity at edge of jet							
inner boundary	e_1	0.61	0.07	1.29	0.61	<	2.23
boundary 2	e_0	0.24	0.12	0.37	0.25	0.14	0.46
Emissivity ratio at inner boundary	g	0.022	0.005	0.036		not used	
B-field							
Boundary positions (kpc)							
inner	ρ_{B_1}	0.92	<	2.95	30.37	18.63	37.46
outer	ρ_{B_0}	8.66	7.20	9.99	38.50	32.55	44.13
RMS field ratios							
radial/toroidal							
inner region	j_1	0.81	0.27	1.38	0.68	<	1.07
outer region	j_0	0.53	0.30	0.72	0.29	<	0.55
longitudinal/toroidal							
inner region	k_1	1.43	1.18	1.74	3.06	2.60	3.62
outer region	k_0	0.11	<	0.26	0.00	<	0.53

^a The Symbol < means that any value smaller than the quoted maximum is allowed.

^b The Symbol > means that any value larger than the quoted minimum is allowed.

^c Undetermined, as the counter-jet is not visible in this region.

5.2 B2 0326+39

5.2.1 Geometry and angle to the line of sight

Our best-fitting model requires an angle to the line of sight of $64^\circ \pm 5^\circ$. The jet is initially well collimated, then flares between 3 and 8 kpc from the nucleus, reaching a maximum opening angle of $\approx 20^\circ$ (Fig. 16a). Further from the nucleus,

it recollimates to a cone with an opening angle of only a few degrees.

5.2.2 Velocity field

The velocity profile along the jet axis is shown by the solid line in Fig. 16(b). The initial velocity of $\beta \approx 0.8$ is maintained within 2 kpc of the nucleus. The jet then decelerates

uniformly out to ≈ 7 kpc from the nucleus, where the velocity reaches its asymptotic value. The data are consistent with a roughly constant velocity of $\beta \approx 0.09$ until the end of the modelled region. There are large fractional uncertainties, since variations in Doppler factor are slight, and we can only set an upper limit of $\beta \lesssim 0.15$ anywhere in this region. We discuss the velocity variations in the outer parts of the jet in more detail in Section 6.2.

The transverse velocity structure is poorly constrained everywhere. In the high-velocity region close to the nucleus, the jet is narrow and poorly resolved transversely. At large z , the jet velocity is low, so differences in sidedness ratio between the centre and edge of the jet, which provide the principal constraint on transverse velocity variations, are undetectably small for our preferred inclination.

5.2.3 Emissivity

The model on-axis profile of $n_0 B^{1+\alpha}$ for B2 0326+39 (derived from the emissivity) is shown by the solid line in Fig 16(c). In general, the profile flattens with increasing z : the fitted power-law indices are 6.1 (< 1.0 kpc), 2.4 (1.0 – 2.7 kpc) and 1.3 (> 3.0 kpc). There are rapid changes in emissivity at 1.0 kpc and 2.8 kpc. The former is explicitly modelled as a discontinuity, with the emissivity changing by a factor of $1/g \approx 40$. The latter, fit by a power-law with a very steep index between 2.7 and 3 kpc, is also consistent with a discontinuity.

In the outer parts of the jet, the emissivity at the jet edge is ≈ 0.25 of its on-axis value with an error of a factor of ≈ 2 . Elsewhere, the jet is poorly resolved transverse to its axis and the off-axis variation is poorly determined.

5.2.4 Magnetic-field structure

Fig. 17 shows profiles of the radial, toroidal and longitudinal components of the magnetic field. As there is no variation with streamline index, these curves apply to all streamlines. The solid lines show our best-fitting model and the shaded areas the allowed errors. Close to the nucleus, the longitudinal component dominates. As the distance from the nucleus increases, this component drops, reaching a value consistent with zero by 8.5 kpc. The largest single component is toroidal from 3.5 kpc onwards, the fraction of radial field remaining roughly constant everywhere. The field structure from 8.5 kpc onwards essentially consists of two-dimensional field sheets aligned perpendicular to the jet axis with a radial/toroidal field ratio ≈ 0.6 . The transverse polarization profiles for the main and counter-jets (Fig. 10) tell slightly different stories about the details of this field configuration. In the main jet, the profile is essentially flat, and is marginally inconsistent with the model prediction of a higher degree of polarization on-axis. It would be slightly better fit by a model in which the toroidal and radial components are equal. The expected polarization for a non-relativistic jet with this field structure at an angle θ to the line of sight is $p = 0.43$ for $\alpha = 0.55$ (Laing 1980). This is slightly less than the observed value, and no transverse variation would be expected. In the counter-jet, the degree of polarization is higher on-axis ($p \approx 0.6$) and there are hints of a decrease towards the edge. Both of these features are better

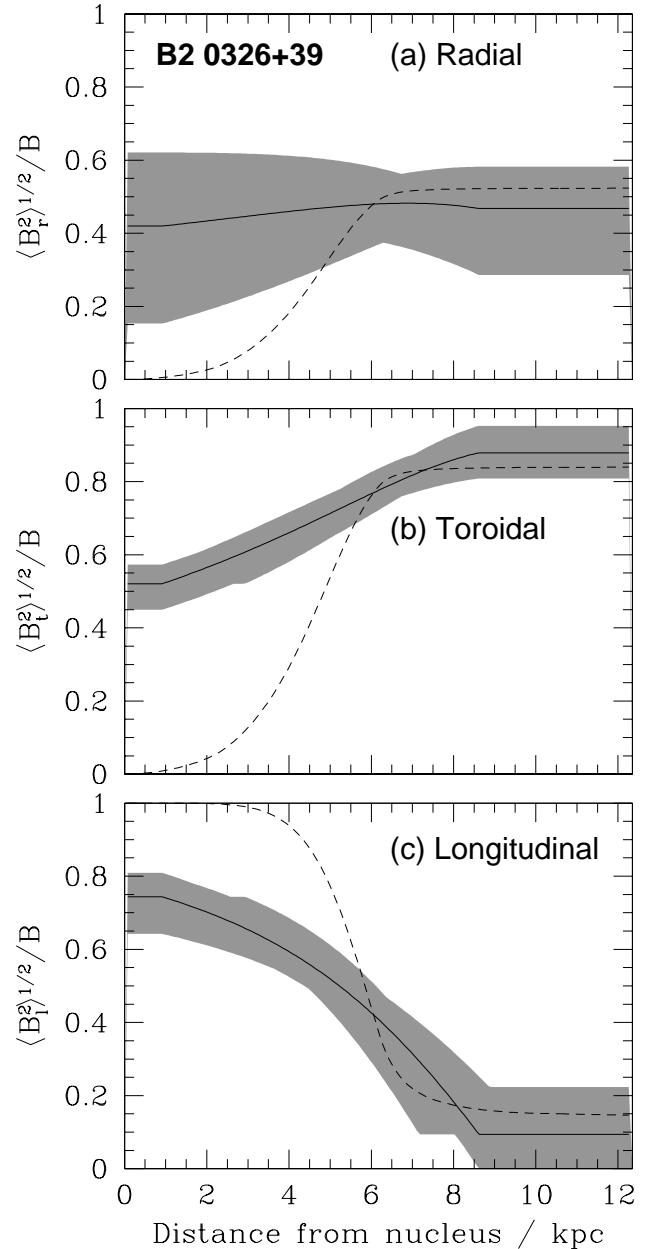


Figure 17. Profiles of: (a) radial, (b) toroidal and (c) longitudinal components of the magnetic field along the streamlines for B2 0326+39. Solid line: best fit model; shaded area: error on the best fit model derived from the limits in Table 6; dashed line: the profile expected on axis, in the absence of shear, if the magnetic field is frozen into the plasma. The latter curves are normalized to match the model at 6 kpc from the nucleus.

fit by increasing the toroidal component. The optimization has compromised between the fits for the two jets to produce the results shown in Fig. 10. It is unclear whether the differences between the field component ratios in the main and counter-jets are real or a product of noisy data.

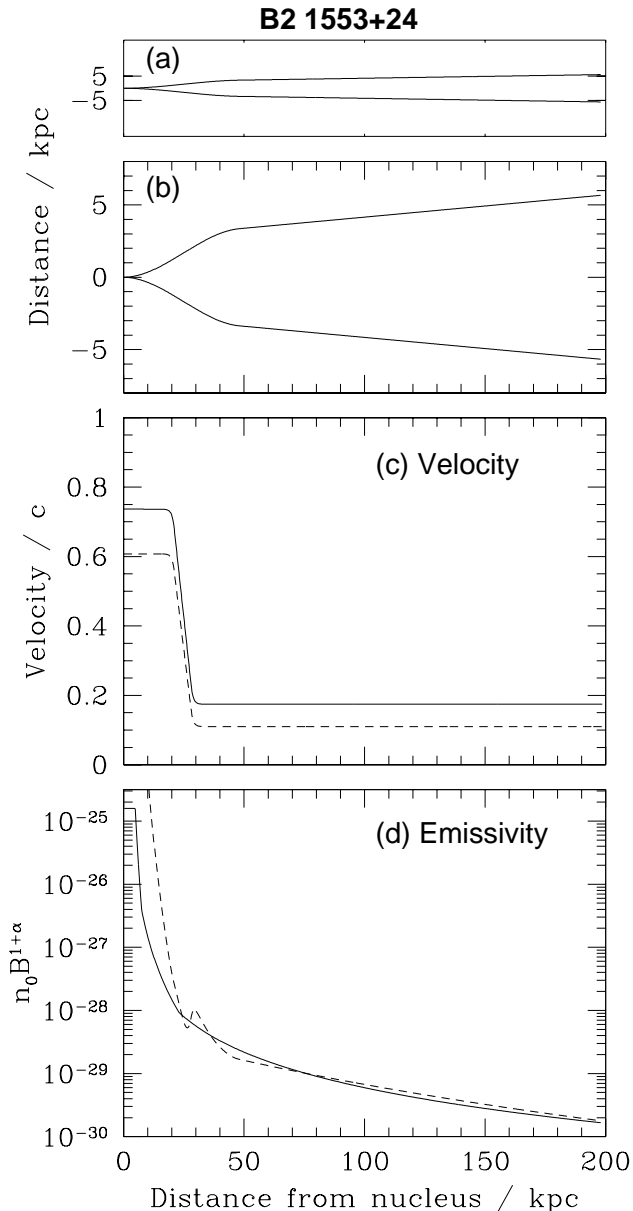


Figure 18. Profiles of intrinsic parameters along the jets of B2 1553+24 in the jet frame. (a) and (b) the shape of the jet edge. Panel (a) shows the jet with equal scales in both axes to give an idea of its real shape. Panel (b) has the width scale expanded by a factor of 6 to illustrate the variations in collimation. (c) the velocity profile along the jet axis (solid line) and jet edge (dashed line). (d) the on-axis profile of $n_0 B^{1+\alpha}$ derived from the emissivity, with n_0 in m^{-3} and B in T. Solid line: model; dashed line, adiabatic approximation with the magnetic-field structure expected from flux freezing, normalized to match the free model at large distances.

5.3 B2 1553+24

5.3.1 Geometry and angle to the line of sight

Our best-fitting model has the jet axis at 7.7° to the line of sight with an error of $\pm 1.3^\circ$. This implies that the jet is has a very narrow ‘pencil’ shape, with a diameter of only ≈ 10 kpc at 200 kpc from the nucleus (Fig. 18a). The jet is well collimated very close to the nucleus, flares to a maxi-

mum opening angle of $\approx 6^\circ$ between 15 and 35 kpc from the nucleus and then recollimates into a cone with an opening angle of $\approx 0.75^\circ$ (Fig 18b).

A near end-on orientation is qualitatively consistent with other measures (Section 2.3) and the source was indeed selected to be close to the line of sight. Nevertheless, the extremely small value of θ implies the existence of a large, missing population of side-on counterparts to B2 1553+24 in the B2 sample. We address this topic in Section 6.3.

5.3.2 Velocity field

Fig. 18(c) shows the model velocity profiles on-axis and at the jet edge ($s = 1$) for B2 1553+24. Within 20 kpc of the nucleus, the data are consistent with a constant value of $\beta = 0.74$, but the counter-jet is invisible in our images and we can only set a limit of $\beta \gtrsim 0.7$. Between 20 and 30 kpc from the nucleus, the jet decelerates very rapidly and at large distances the velocity tends to an asymptotic value of $\beta = 0.17 \pm 0.04$.

The variation in velocity transverse to the jet axis close to the nucleus is only constrained by the lack of a visible counter-jet, which indicates that the velocity at the jet edge must be $\beta > 0.5$ (> 0.7 times the on-axis value). Further from the nucleus, our best-fitting model has a ratio of edge to on-axis velocity ≈ 0.6 , although the error is high. As in B2 0326+29, the velocities are too low to produce significant variations in Doppler factor across the jets unless the edge/on-axis ratio $\lesssim 0.2$.

5.3.3 Emissivity

The on-axis profile of $n_0 B^{1+\alpha}$ is shown by the solid line in Fig. 18(d). Within ≈ 5 kpc of the nucleus the emissivity is constant, the dramatic brightening of the jet in this region being produced by the rapid expansion alone: no discontinuity is required. Further from the nucleus, the profile falls as a power-law, initially very steeply (index ≈ 8) but flattening off as the distance increases. Between the start of the emissivity decrease and the end of the modelled region the emissivity drops by five orders of magnitude. In the regions of the jet where we have adequate transverse resolution, the emissivity falls to ≈ 0.25 of its on-axis value at the jet edge with an error of roughly a factor of two.

5.3.4 Magnetic-field structure

Profiles of the rms field components along the jets are shown by the solid lines in Fig. 19. As in B2 0326+39, there is no variation with streamline index. The shaded areas show the variations allowed by the error estimates in Table 6. Within 30 kpc of the nucleus, the field is mostly longitudinal; between 30 and 40 kpc there is a rapid transition to a toroidally dominated structure which is maintained over the rest of the modelled region (although the error estimates do allow a significant proportion of longitudinal field to remain). The best fit for the fractional radial component is close to a constant value of ≈ 0.2 , but the data are also consistent with a complete absence of radial field. A pure toroidal field would fit the polarization data for $z > 40$ kpc.

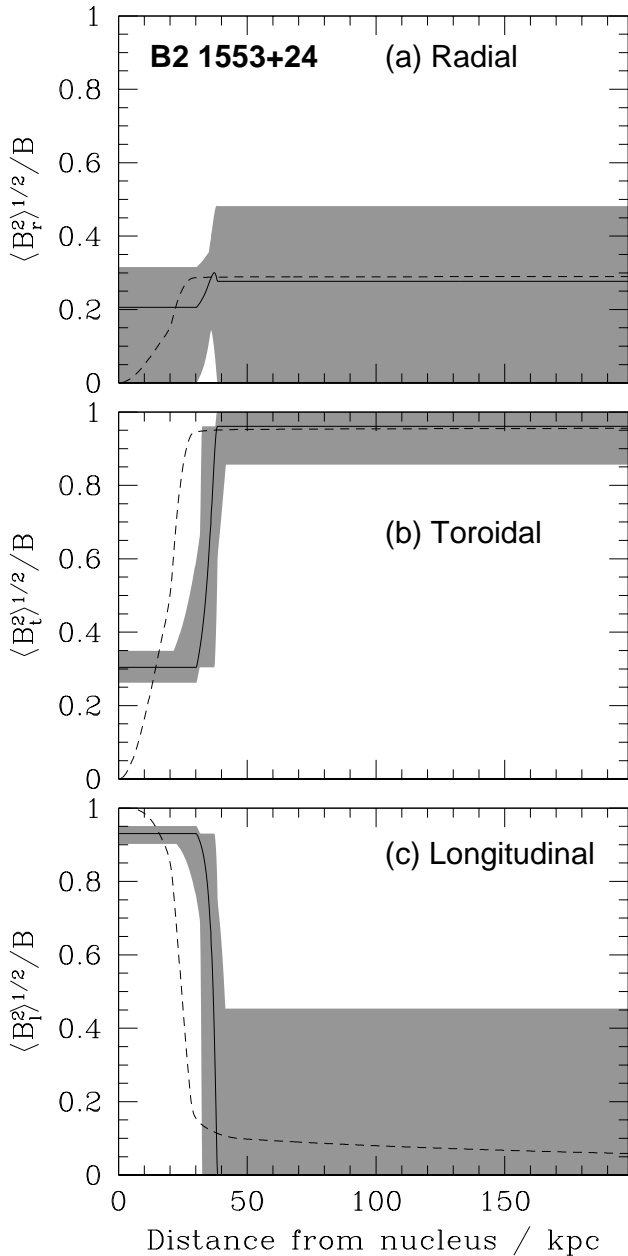


Figure 19. Profiles of (a) radial, (b) toroidal and (c) longitudinal components of the magnetic field along the streamlines in B2 1553+24. Solid line: best-fitting model; shaded area: error on the model derived from the limits in Table 6; dashed line: profile expected on-axis, in the absence of shear if the magnetic field is frozen into the plasma. The latter curves are normalized to match the model values at 38 kpc from the nucleus.

6 DISCUSSION

6.1 Adiabatic models

The simplest physical picture of the evolution of the emissivity along a jet assumes that the radiating particles only lose energy adiabatically (synchrotron and inverse-Compton losses being negligible by comparison), that there are no dissipative processes such as particle acceleration or field-line reconnection, and that the magnetic field is convected passively with the (laminar) flow. Analytical equations for the

emissivity in this case were first derived by Burch (1979); these were generalized by Baum et al. (1997) to describe a relativistic, decelerating flow with purely perpendicular or parallel field. We use the latter expressions, modified to calculate the magnetic-field evolution self-consistently as in Laing & Bridle (2004), to estimate the emissivity profiles expected for our models of jet shape and velocity.

We refer to the fits derived in the previous sections and by LB as *free models* in order to distinguish them from *adiabatic models*, following the terminology of Laing & Bridle (2004).

6.1.1 Magnetic-field profiles

Baum et al. (1997) showed that the variations of the magnetic field components in the quasi-one-dimensional approximation are:

$$\begin{aligned} B_r &\propto (x\beta\Gamma)^{-1} \\ B_t &\propto (x\beta\Gamma)^{-1} \\ B_l &\propto x^{-2} \end{aligned}$$

in the absence of shear (x is again the jet radius). Given the field components at one point in the jet, we can then predict their evolution from the profiles of radius and velocity given in the previous section.

The predicted evolution of the field components in B2 0326+39 and B2 1553+24 is shown by the dashed lines in Figs 17 and 19, respectively. The initial conditions have been chosen to match the free models at the distances from the nucleus given in the figure captions (note that the field is forced to be longitudinal at the nucleus).

The qualitative evolution of the field components is consistent with the free models for both sources: a decrease in the longitudinal component is accompanied by an increase in the toroidal component. Rapid flaring and deceleration act in the same sense, leading to a large decrease in the relative fraction of longitudinal field, as observed. There are significant quantitative discrepancies, however, particularly in the regions where the jets decelerate. In both sources, the transition from longitudinal to transverse field is predicted to be less abrupt than is seen in the free models. This discrepancy is qualitatively consistent with the effects of velocity shear due to a transverse velocity gradient, which will act to increase the longitudinal component and to delay the onset of the longitudinal to transverse transition. This cannot be the whole story, however, as there are also large differences between the variations of the toroidal and radial components. The former increases, as expected, but the latter stays roughly constant: in the quasi-one-dimensional approximation, their ratio should remain constant. Similar problems occur in 3C 31 (LB; Laing & Bridle 2004).

Komissarov & Ovchinnikov (1989, 1990) showed that the variation of the rms toroidal and longitudinal field components with distance could be very different from that predicted by the simple adiabatic approximation if the flow is turbulent, as is widely believed (e.g. Bicknell 1984; De Young 1996). Given that the gross departures from the flux-freezing predictions occur where the jets are fast, or are decelerating rapidly, it seems likely that turbulence affects

both the magnitude and the configuration of the field in these regions.

6.1.2 Emissivity profiles

The emissivity function ϵ can be written in terms of the magnetic field B , both as defined in Section 3.6, as:

$$\epsilon \propto (x^2 \beta \Gamma)^{-(1+2\alpha/3)} B^{1+\alpha}$$

(Baum et al. 1997; Laing & Bridle 2004). B can be expressed in terms of the parallel-field fraction $f = \langle B_{\parallel}^2 \rangle^{1/2} / B$ and the radius \bar{x} , velocity $\bar{\beta}$ and Lorentz factor $\bar{\Gamma}$ at some starting location using equation 8 of Laing & Bridle (2004):

$$B \propto \left[f^2 \left(\frac{\bar{x}}{x} \right)^4 + (1 - f^2) \left(\frac{\bar{\Gamma} \bar{\beta} \bar{x}}{\Gamma \beta x} \right)^2 \right]^{1/2}$$

We can therefore predict the emissivity using our fitted jet width and velocity together with an estimate of the parallel-field fraction f . The resulting emissivity profiles for B2 0326+39 and B2 1553+24 are shown in Figs 16(c) and 18(d), respectively. The solid lines show the emissivity profiles from our free model fits and the dashed lines the self-consistent adiabatic profiles, normalized to match at large z .

In both objects the adiabatic models agree poorly with the free models where the jet velocities are high. The emissivity falls off much too rapidly in the adiabatic models, just as in 3C 31 (LB). This is not a surprise, for the following reasons:

- (i) Velocity shear (required by the free model) has been neglected.
- (ii) The magnetic-field evolution is more complicated than expected from simple flux-freezing in an axisymmetric laminar-flow model, even if shear is included (Section 6.1.1) and turbulence may dominate the field evolution (Komissarov & Ovchinnikov 1989, 1990).
- (iii) Where the jets are fast, we see complex, small-scale, non-axisymmetric structures, indicating that the flow is not laminar.
- (iv) In B2 1553+24, there is optical synchrotron emission from the base of the main jet (Parma et al. 2003), implying continuing particle acceleration.

Further from the nucleus, where the velocity has a low and roughly constant value, the adiabatic profile matches the free model very well in both objects. In B2 0326+39 this is within a region 4 to 12 kpc (Fig. 16). In B2 1553+24, the region of low, constant velocity extends from 30 to 200 kpc and the adiabatic profile agrees very well with the free model over approximately 1.5 orders of magnitude in emissivity (Fig. 18). This suggests that the outer jets in this source are modelled surprisingly well as constant-velocity, perpendicular-field, adiabatically-evolving flows.

6.2 Sidedness profiles and reacceleration

Our models, motivated by the gross features of the observed sidedness ratios, assume monotonic deceleration. There are theoretical reasons to expect jets to be reaccelerated by the pressure gradient of the external medium at large distances

from the nucleus provided that the mass injection rate is not too large, for example if stellar mass loss dominates the mass injection (Komissarov 1994; Bowman, Leahy & Komissarov 1996). The most obvious effect of reacceleration is a small increase of sidedness ratio with distance from the nucleus. No such increase is obvious from the ridge-line profiles or images of sidedness ratio (Figs 6 and 13). We have therefore averaged the sidedness ratios in rings of constant distance from the nucleus in order to improve the signal-to-noise ratio (Fig. 20).

This reveals considerable sidedness structure in the low-velocity regions. Both sources show sidedness minima, at ≈ 14 kpc from the nucleus in B2 0326+29 and at ≈ 8 kpc in B2 1553+24. The minimum for B2 0326+39 occurs roughly where Worrall & Birkinshaw (2000) inferred that the synchrotron minimum pressure in the jets (Bridle et al. 1991) becomes less than the pressure of the external medium.

Fig. 20 shows the average observed sidednesses as solid lines and our best-fitting models as dashed lines. The dotted lines show the profiles for models with the outer velocity parameters, β_0 , modified to fit the minimum and maximum sections of the observed profiles in the outer region. The velocity ranges are $\beta_0 = 0.03 - 0.25$ for B2 0326+39 and $0.13 - 0.19$ for B2 1553+24. [Note that the model sidedness profiles increase slightly with distance from the nucleus because progressively larger areas of jet edge, which have lower sidedness ratios than the centres, fall below the intensity blanking threshold].

If the changes in sidedness result from acceleration, then they should be associated with variations in the degree of polarization. In B2 0326+39, the field structure can be roughly approximated by two-dimensional field sheets with equal radial and toroidal components (Section 5.2.4). The expected changes in polarization are then straightforward to calculate (Laing 1980). For an acceleration from $\beta = 0.03$ to $\beta = 0.25$ between 16 and 18 arcsec from the nucleus, as implied by a naive interpretation of Fig. 20(a), p should vary from 0.49 to 0.64 in the main jet and from 0.45 to 0.38 in the counter-jet. These changes are not observed (Figs 7e and 8). The velocity increase is far larger than is expected from the effects of any pressure gradient in the external medium and we also note that the fit of an accelerating adiabatic model to the emissivity profile would be significantly worse than that shown in Fig. 16.

In B2 1553+24, it is more difficult to exclude acceleration as the cause of the increase in sidedness ratio between 8 and 14 arcsec from the nucleus (Fig. 20b): the predicted variations in degree of polarization are below the fluctuation level in Fig. 14(e) and we cannot average across the jet to reduce the noise; the velocity increase required ($\beta_0 = 0.13 - 0.19$) is physically more reasonable than in B2 0326+39 and the adiabatic model fit to the emissivity is comparable in quality to that in Fig. 18.

We conclude that there is no compelling evidence in favour of reacceleration of the jets in either source, and that it is most unlikely to be the sole cause of the increase in sidedness ratio with distance from the nucleus in B2 0326+39. Nevertheless, it is expected theoretically, there are hints that it might occur, and it is consistent with the total intensity and polarization data in B2 1553+24.

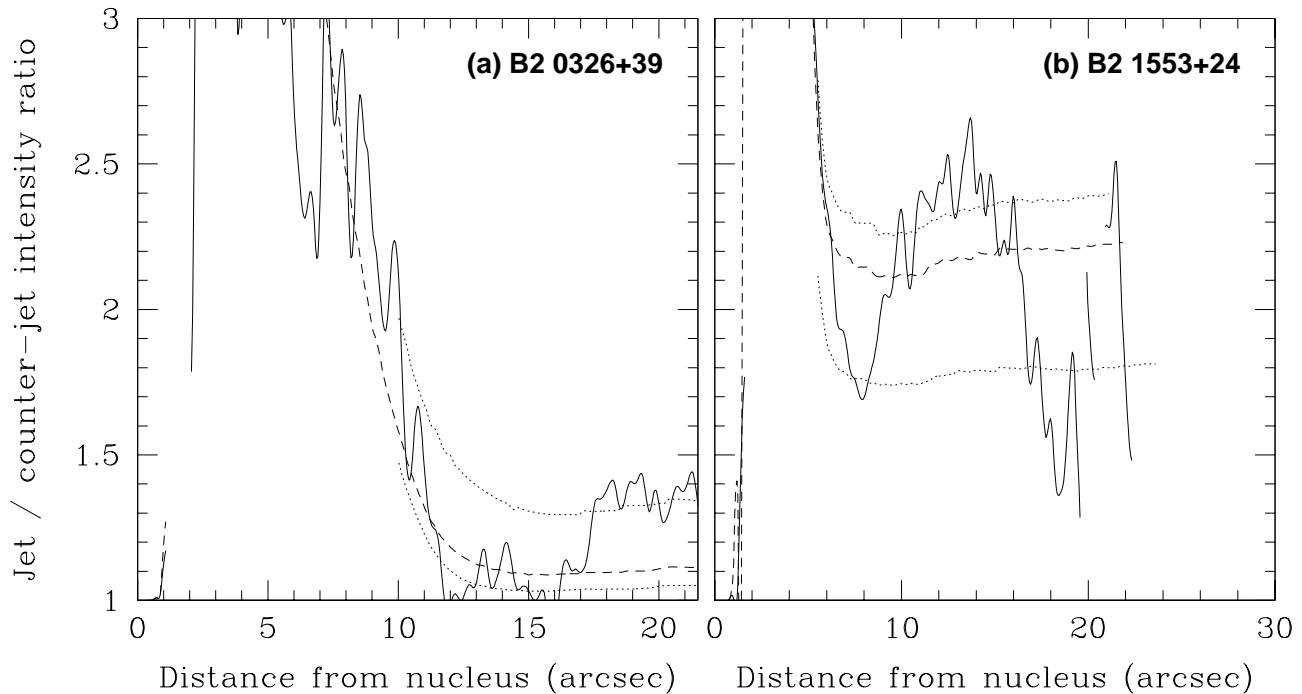


Figure 20. Sidedness profiles of: (a) B2 0326+39 at 0.5 arcsec resolution and (b) B2 1553+24 at 0.75 arcsec resolution, averaging over all points at the same distance from the nucleus. Solid line: data; dashed line: best fit model; dotted lines: models with β_0 modified to fit the minimum and maximum sidednesses in the lower-velocity region, as described in the text.

6.3 The appearance of B2 1553+24 at other angles to the line of sight

We infer that the angle to the line of sight for B2 1553+24 is $\approx 8^\circ$. Given that the B2 sample from which it is drawn is selected at the low frequency of 408 MHz, the usual assumption is that the emission is isotropic and therefore that the distribution of jet orientations for its members should be random. The source should therefore have many (~ 100) counterparts of comparable total luminosity and larger θ , but the entire sample of B2 radio galaxies with jets defined in Tables 1 and 2 of Parma et al. (1987) has 43 members. A further concern is that the counterparts must be very large. The length of the main jet is at least 60 arcsec (Fig. 2a), corresponding to 388 arcsec (340 kpc) at $\theta = 60^\circ$, the median angle to the line of sight. This is comparable in size with the longest jet in the sample, in NGC 315 (Willis et al. 1981), and far larger than the median (≈ 30 kpc; Parma et al. 1987). There is cause for suspicion unless: (a) the side-on counterparts of B2 1553+24 are not members of the B2 sample or (b) sources in that sample have linear sizes far larger than previously realised.

In order to understand potential selection effects, we have computed the appearance of the model brightness distribution for B2 1553+24 at various angles to the line of sight. We show the results for the median angle to the line of sight for an isotropic sample ($\theta = 60^\circ$) and for a source in the plane of the sky ($\theta = 90^\circ$) in Fig. 21. The area chosen for the plots corresponds to the modelled region for the 60° case. As well as being very long, the jets appear narrow, straight and (except for a small region around the nucleus) extremely faint. The total flux density from the inner 200 kpc of the model jets (measured along the jets and excluding the

core) is constrained to be 44 mJy for the $\theta = 7.7^\circ$ model but is 27 mJy for $\theta = 60^\circ$. There are three important selection effects:

(i) The extended flux of the jets shows significant Doppler boosting at small θ . Given that there is little lobe emission in B2 1553+24 (de Ruiter et al. 1993; Condon et al. 1998), the jets probably dominate the flux at low radio frequencies, so end-on sources of this type will be selected preferentially in the B2 survey. The integral source count $N(> S) \propto S^{-3/2}$ for the luminosities and redshifts in question, so the size of the parent sample is effectively increased by a factor of $(44/27)^{3/2} \approx 2$ if isotropic lobe emission is ignored.

(ii) Except for a small region around the nucleus, the model jets are faint. Further than 50 arcsec from the nucleus, the surface brightness is $\lesssim 0.16$ mJy/beam area at 8.4 GHz with a beam of 2.75 arcsec FWHM. This scales to 0.47 mJy/beam area at 1.4 GHz for a spectral index $\alpha = 0.6$, comparable with the detection threshold for typical VLA images of sources in the sample presented by Fanti et al. (1986, 1987). In any case, emission on scales $\gtrsim 120$ arcsec would not have been imaged reliably in existing VLA observations of the B2 sample (C configuration at 1.4 GHz; Fanti et al. 1987). The combination of these two effects makes it extremely unlikely that the outer jets would have been detected.

(iii) Sources of large angular size with flux densities close to the limit of the catalogue could have been missed by the original B2 survey, which measured peak rather than integrated flux density. We have estimated the magnitude of this effect by convolving the model brightness distribution for $\theta = 60^\circ$ with the beam of the B2 survey (3×10 arcmin²). If the short axis of the beam is parallel to the jet axis, the

ratio of peak/total flux is 0.73; if the long axis of the beam is aligned, the ratio becomes 0.95. A few sources could therefore have been missed (primarily those orientated E-W).

We conclude that the side-on counterparts of B2 1553+24 could have escaped identification, either because they were missed in the original survey or because their angular sizes have been greatly underestimated. Morganti & Parma (private communication) and Ledlow & Owen (2004; in preparation) have made more sensitive observations of radio galaxies in the B2 sample using the WSRT and the VLA in D configuration and have shown that a significant fraction of them have much longer radio jets than have previously been reported, extending many 100's of kpc or even further. We suggest that these form part of the missing population.

6.4 Similarities and differences between B2 0326+39, B2 1553+24 and 3C 31

In later papers, we will present a re-analysis of 3C 31 along with models of two further objects, all with the same functional descriptions of velocity, emissivity and magnetic field. This will allow a full comparison between them; here we make a few general observations about the similarities and differences between B2 0326+39, B2 1553+24 and 3C 31.

Notable similarities are:

- (i) All three objects can be modelled successfully by a decelerating jet model.
- (ii) The jets are all initially well collimated, then flare before recollimating and expanding conically.
- (iii) Close to the nucleus the jet velocity on-axis is consistent with a value of $\beta \approx 0.8$ in all cases.
- (iv) Deceleration occurs over a region of ≈ 10 kpc to an outer velocity of $0.0 \lesssim \beta \lesssim 0.2$.
- (v) The ratio of edge to on-axis velocity is consistent with a constant value of ≈ 0.7 everywhere, although in some places this is poorly constrained.
- (vi) The exponent of the emissivity index is similar in the outermost modelled regions of all the jets.
- (vii) At the jet edge the emissivity falls to ≈ 0.25 of its on-axis value.
- (viii) The longitudinal field component dominates in the high-velocity regions close to the nucleus and the toroidal component in the outer parts, qualitatively but not quantitatively as expected from flux freezing.
- (ix) The variation of the radial field component is more complex than predicted by simple flux-freezing models. This effect cannot simply be due to velocity shear in a laminar, axisymmetric flow.
- (x) Close to the nucleus (in the high-velocity and deceleration regions), the variation of emissivity with distance from the nucleus is far less rapid than predicted by the adiabatic approximation.
- (xi) In the low-velocity outer regions, the emissivity variation is reasonably well fitted by a quasi-one-dimensional adiabatic model.

The three objects were expected to have a wide range of angles to the line of sight; this is confirmed by our modelling. In addition, there are some clear differences:

- (i) The conical outer region of 3C 31 has a large opening angle and is centred on the nucleus. The outer regions

of the other two objects are closer to cylindrical, with very small opening angles and vertices far behind the nucleus. [Note that 3C 31 does recollimate outside the modelled region (LB)].

- (ii) The velocity in the outer region of 3C 31 was modelled by LB as decreasing monotonically with distance from the nucleus (as required by the variation of sidedness ratio). In the B2 sources, it has an approximately constant asymptotic value.

(iii) The close connection between the jet geometry and the forms of the velocity and emissivity profiles inferred for 3C 31 is not general.

- (iv) The velocity in B2 1553+24 remains at $\beta \approx 0.8$ until ≈ 20 kpc from the nucleus (cf. ≈ 2 kpc in the other two objects).

(v) There is no need for a discontinuity in emissivity in B2 1553+24: the brightening of the jet is consistent with expansion at constant emissivity.

(vi) Although the biggest single field component at large distances is always toroidal, there are significant differences in the details of the field-component evolution: 3C 31 has a mixture of longitudinal and toroidal components; B2 0326+39 has toroidal and radial components and B2 1553+24 has almost pure toroidal field.

(vii) In 3C 31, the radial field component in the flaring region increases towards the edge of the jet. There is no evidence for this effect in the B2 sources, although it cannot be excluded in B2 0326+39, where the signal-to-noise ratio is low.

(viii) The adiabatic approximation describes the emissivity evolution in B2,1553+24 over a much larger fraction of the jets than in the other two sources. This may be because it applies most accurately in the low-velocity outer region, which is relatively longer in this source.

7 SUMMARY AND FURTHER WORK

7.1 Summary

7.1.1 General

We have shown that the total and linearly-polarized synchrotron emission from the jets of the FRI radio galaxies B2 0326+39 and B2 1553+24 can be modelled successfully on the assumption that they are axisymmetric, intrinsically symmetrical, relativistic, decelerating flows. The models are based on those developed by LB for 3C 31, with modifications to the functional forms assumed for geometry, velocity, emissivity and magnetic field. In particular, we found that the variations of intrinsic parameters were not directly coupled to the geometry of the jets as defined by their outer isophotes.

7.1.2 Geometry

In the *flaring region* close to the nucleus, the jet radius x can be fitted by a polynomial of the form $x = a_2 z^2 + a_3 z^3$, where z is the distance from the nucleus. In the *outer region* at larger distances, the jets are conical, with opening angles sufficiently small that they are almost cylindrical. The inferred angles to the line of sight are $64^\circ \pm 5^\circ$ for B2 0326+39 and $7.7^\circ \pm 1.3^\circ$ for B2 1553+24.

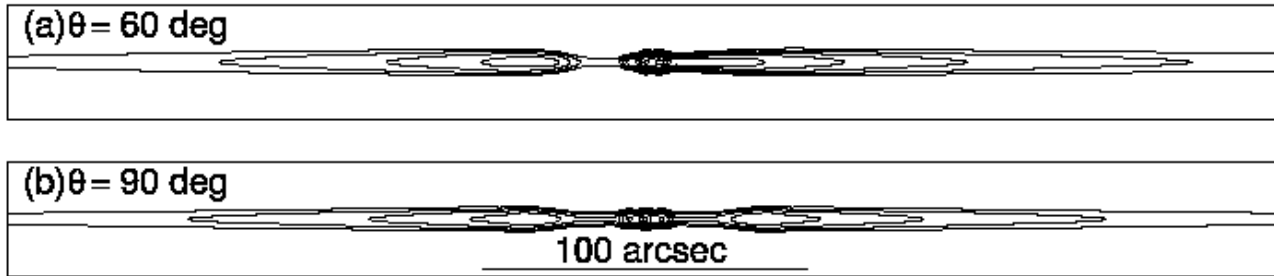


Figure 21. The brightness distribution of the model for the jets in B2 1553+24 at angles to the line of sight of: (a) $\theta = 60^\circ$ and (b) $\theta = 90^\circ$. The plots cover 394 arcsec (346 kpc) in projection on the sky. This corresponds to a distance from the nucleus along the jet axis of 200 kpc in both directions for $\theta = 60^\circ$, i.e. to the size of the modelled region. The contour levels are 1, 2, 4, 8, 16, 32, 64, 128, 256, $512 \times 20\mu\text{Jy}/\text{beam}$ and the model images have been convolved with a 2.75-arcsec Gaussian beam.

7.1.3 Velocity

Close to the nucleus the jets have high and approximately constant velocities $\beta \approx 0.8$. They decelerate rapidly over distances of < 10 kpc to a constant asymptotic outer velocities $\beta \lesssim 0.2$. The velocities at the jet edges are consistent with ≈ 0.7 of their on-axis values everywhere.

7.1.4 Emissivity

The emissivity profiles along the jets can be divided into discrete regions, each with a power-law variation. The power-laws tend to be flatter further from the nucleus, although regions close to the nucleus (where knots of emission are seen) are modelled as bright plateaux with rapid decreases in emissivity at their ends. In the low-velocity regions after the jets have decelerated, the emissivity profiles are consistent with a simple, quasi-one-dimensional adiabatic model; closer to the nucleus, the adiabatic approximation predicts too steep a decline of emissivity with distance. The fractional emissivity at the edge of the jets is ≈ 0.25 everywhere.

7.1.5 Magnetic Field

Although the observed polarization structures of the two objects appear radically different, the main features of the magnetic-field evolution are similar in both cases: the principal differences result from projection. In both objects, the field is dominated by the longitudinal component in the region close to the nucleus; further out, the largest single component is toroidal. The radial field components are ≈ 0.4 and ≈ 0.2 of the total in B2 0326+39 and B2 1553+24, respectively. No evidence for transverse structure in the field-component ratios is seen in either source. Evolution from longitudinal to transverse field is qualitatively consistent with flux-freezing in an expanding, decelerating jet, but there are complications. First, the ratio of radial to toroidal field (which should remain roughly constant even if there is velocity shear) varies significantly along the jets. Second, the details of the component evolution are quantitatively inconsistent with the flux-freezing picture.

7.2 Further work

We have modelled 3C 31 with the modified functional descriptions used here in order to allow a quantitative com-

parison with other objects. As expected from the variation of sidedness ratio with distance from the nucleus (LB), the jet velocity in 3C 31 does not reach an asymptotic value in the modelled region. We have shown, however, that use of the new velocity law allows as good a fit to the observations as that achieved by LB and that their conclusions are not significantly modified. We have also successfully applied the model to the well-known radio galaxies NGC 315 (Venturi et al. 1993) and 3C 296 (Harcastle et al. 1997). These results will be presented in future papers.

When suitable X-ray observations are available, we will apply the conservation-law approach developed by Laing & Bridle (2002b) to infer the energy and momentum fluxes of the modelled jets and their variations of pressure, density and entrainment rate with distance from the nucleus. Our eventual aim is to replace the empirical descriptions of internal quantities with more physically derived ones. Initially, we will apply the more sophisticated adiabatic model developed by Laing & Bridle (2004) to the outer regions of the jets and in particular to B2 1553+24, where the simple analysis of Section 6.1 suggests that the adiabatic approximation holds over a large range of distances. We then plan to incorporate the effects of synchrotron and inverse Compton losses in a self-consistent way, to model the observed emission from radio to X-ray wavelengths and to quantify the particle-acceleration processes in FRI radio jets.

ACKNOWLEDGMENTS

JRC acknowledges a research studentship from the UK Particle Physics and Astronomy Research Council (PPARC). The National Radio Astronomy Observatory is a facility of the National Science Foundation operated under cooperative agreement by Associated Universities, Inc. We thank Paola Parma, Raffaella Morganti, Frazer Owen and Michael Ledlow for communicating results in advance of publication, Alan Bridle for comments on the text and the referee for constructive suggestions.

REFERENCES

- Baum S.A., O’Dea C.P., Giovannini G., Biretta J., Cotton W.B., de Koff S., Feretti L., Golombek D., Lara L., Macchetto F.D., Miley G.K., Sparks W.B., Venturi T.,

- Komissarov S.S., 1997, *ApJ*, 483, 178 (erratum *ApJ*, 492, 854)
- Begelman, M.C., Blandford, R.D., Rees, M.J., 1984, *Rev. Mod. Phys.*, 56, 255
- Bicknell, G. V., 1984, *ApJ*, 286, 68
- Bicknell G.V., 1994, *ApJ*, 422, 542
- Biretta J.A., Zhou F., Owen F.N., 1995, *ApJ*, 447, 582
- Bondi M., Parma P., de Ruiter H.R., Laing R.A., Fomalont E.B., 2000, *MNRAS*, 314, 11
- Bowman M., Leahy J.P., Komissarov S.S., 1996, *MNRAS*, 279, 899
- Bridle A.H., 1982, in: *Extragalactic Radio Sources*, Proc. I.A.U. Symp 97, eds D.S. Heeschen, C.M. Wade, Reidel, Dordrecht, P. 121
- Bridle A.H., Perley R.A., 1984, *ARA&A*, 22, 319
- Bridle A., Baum S., Fomalont E., Fanti R., Parma P., Ekers R., 1991, *A&A*, 245, 371
- Burch S.F., 1979, *MNRAS*, 187, 187
- Canosa C.M., Worrall D.M., Hardcastle M.J., Birkinshaw M., 1999, *MNRAS*, 310, 30
- Capetti A., de Ruiter H.R., Fanti R., Morganti R., Parma P., Ulrich M.-H., 2000, *A&A*, 362, 871
- Colla, G., Fanti, C., Ficarra, A., Formiggini, L., Gandolfi, E., Grueff, G., Lari, C., Padrielli, L., Roffi, G., Tomasi, P., Vigotti, M., 1970, *A&AS*, 1, 281
- Colla G., Fanti C., Fanti R., Gioia I., Lari C., Lequeux J., Lucas R., Ulrich M.-H., 1975, *A&AS*, 20, 1
- Condon, J.J., Cotton, W.D., Greisen, E.W., Yin, Q.E., Perlay, R.A., Taylor, G.B., Broderick, J.J., 1998, *AJ*, 115, 1693
- De Young, D. S., 1996, in Hardee, P.E., Bridle, A.H., Zensus, J.A., eds, *ASP Conf. Series 100, Energy Transport in Radio Galaxies and Quasars*, ASP, San Francisco, p. 261
- de Ruiter, H.R., Capetti, S., Morganti, R., Parma, P., Lazari, L., Fanti, R., 1993, in *Lecture Notes in Physics 421: Jets in Extragalactic Radio Sources*, eds Röser, H.-J., Meisenheimer, K., Springer-Verlag, Berlin, 21
- Fanaroff B.L., Riley J.M., 1974, *MNRAS*, 167, 31P
- Fanti R., Gioia I., Lari C., Ulrich M.-H., 1978, *A&AS*, 34, 341
- Fanti C., Fanti R., de Ruiter H.R., Parma P., 1986, *A&AS*, 65, 145
- Fanti C., Fanti R., de Ruiter H.R., Parma P., 1987, *A&AS*, 69, 57
- Giovannini G., Cotton W.D., Feretti L., Lara L., Venturi T., 2001, *ApJ*, 552, 508
- Hardcastle M.J., Alexander P., Pooley G.G., Riley J.M., 1997, *MNRAS*, 288, L1
- Hardcastle M.J., Worrall D.M., Birkinshaw M., Laing R.A., Bridle A.H., 2002, *MNRAS*, 334, 182
- Komissarov S.S., 1994, *MNRAS*, 269, 394
- Komissarov, S.S., Ovchinnikov, I.L., 1989, *Sov. Astron.*, 33, 514
- Komissarov, S.S., Ovchinnikov, I.L., 1990, *Sov. Astron. Lett.*, 16, 119
- Laing R.A., 1980, *MNRAS*, 193, 439
- Laing R.A., 1981, *ApJ*, 248, 87
- Laing R.A., 1988, *Nature*, 331, 149
- Laing R.A., 2002, *MNRAS*, 329, 417
- Laing R.A., Bridle A.H., 2002a, *MNRAS*, 336, 328 (LB)
- Laing R.A., Bridle A.H., 2002b, *MNRAS*, 336, 1161
- Laing R.A., Bridle A.H., 2004, *MNRAS*, 348, 1459
- Laing R.A., Parma P., de Ruiter, H.R., Fanti R., 1999, *MNRAS*, 306, 513
- Miller N., Ledlow M., Owen F., Hill J., 2002, *AJ*, 123, 3018
- Morganti R., Fanti C., Fanti R., Parma P., de Ruiter H. R., 1987, *A&A*, 183, 203
- Morganti R., Parma P., Capetti A., Fanti R., de Ruiter H.R., Prandoni, I., 1997a, *A&AS*, 126, 335
- Morganti R., Parma P., Capetti A., Fanti R., de Ruiter H.R., 1997b, *A&A*, 326, 919
- Parma P., 1982, in *Extragalactic Radio Sources*, Proc. I.A.U. Symp 97, eds D.S. Heeschen, C.M. Wade, Reidel, Dordrecht, 193
- Parma P., de Ruiter H.R., Fanti C., Fanti R., Morganti R., 1987, *A&A*, 181, 244
- Parma P., de Ruiter H.R., Capetti A., Fanti R., Morganti R., Bondi M., Laing R.A., Canvin J.R., 2003, *A&A*, 397, 127
- Press W.H., Teukolsky S.A., Vetterling W.T., Flannery B.P., 1992, *Numerical Recipes*, Cambridge University Press, Cambridge.
- Stocke J.T., Burns J.O., 1987, *ApJ*, 319, 671
- Urry C.M., Padovani P., 1995, *PASP*, 107, 803
- Venturi T., Giovannini G., Feretti L., Comoretto G., Wehrle A.E., 1993, *ApJ*, 408, 81
- Wardle J.F.C., Kronberg P.P., 1974, *ApJ*, 194, 249
- Willis A.G., Strom R.G., Bridle A.H., Fomalont E.B., 1981, *A&A*, 122, 305
- Worrall D.M., Birkinshaw M., 2000, *ApJ*, 530, 719